Evaluation of Polar WRF forecasts on the Arctic System Reanalysis Domain:
2. Atmospheric hydrologic cycle

Aaron B. Wilson,[1,2] David H. Bromwich,[1,2] and Keith M. Hines[1]

[1]   The forecast atmospheric hydrologic cycle of the Polar version 3.1.1 of the Weather Research and Forecasting model (WRF) is examined for December 2006 – November 2007. The domain is similar to the Arctic System Reanalysis (ASR), an assimilation of model fields and Arctic observations being conducted partly by the Byrd Polar Research Center. Simulations are performed in 48 h increments initialized daily at 0000 UTC, with the first 24 h discarded for model spin-up of the hydrologic cycle and boundary layer processes. Precipitation analysis reveals a negative annual mean bias (-9.4%) in the polar region, with particularly dry station biases reflected in the Canadian Archipelago. Annual mean bias for the midlatitudes is small and positive (4.6%), attributed to excessive precipitation during spring and summer when convective precipitation is dominant. An examination of precipitation within four major Arctic river basins shows large positive biases due to excessive convective precipitation in summer as well, but highlights the Arctic climate's strong dependence on midlatitude precipitation. Nudging the model's boundary layer moisture toward drier conditions decreases convective precipitation improving the prediction. Cloud fraction analysis shows too little cloud cover, supported by an excess in incident shortwave radiation and a deficit in downwelling longwave radiation throughout the domain. The longwave bias is present regardless of the amount of cloud water or cloud ice, demonstrating a need to improve cloud effects on radiation in Polar WRF. This examination provides a benchmark of the forecast atmospheric hydrological cycle of Polar WRF and its use as ASR's primary model.

1.   Introduction

[2] Following from the Study of Environmental Arctic Change (SEARCH) [*Arctic Research Consortium of the United States*, 2005], the Arctic System Reanalysis (ASR) is being performed partly by the Polar Meteorology Group of the Byrd Polar Research Center at The Ohio State University. ASR is the merging of historical atmospheric, oceanic, land surface, and cryosphere observations using data assimilation techniques and regional modeling with the goal of enhanced understanding of the changing coupled Arctic atmosphere-sea-ice-land system [*Bromwich et al.*, 2010].

[3] The use of the Weather Research and Forecasting (WRF) model for polar applications has been well demonstrated including high resolution modeling of cloud microphysics [*Solomon et al.*, 2009], wintertime inversions in interior Alaska [*Mölders and Kramm*, 2010], and boundary layer winds in areas of complex terrain [*Kipeläinen et al.*, 2011; *Mäkiranta et al.*, 2011]. Optimization of the WRF model for use in polar regions (Polar WRF) has been ongoing as well, with the intent to design a mesoscale model suitable for Arctic applications including the primary model for ASR. Specifically, Polar WRF has been tested on the Greenland ice sheet using version 2.1.1 [*Hines and Bromwich*, 2008], over the Arctic Ocean with version 2.2 [*Bromwich et al.*, 2009], and on Arctic land using version 3.0.1.1 [*Hines et al.*, 2011]. Polar modifications to WRF include updates to surface longwave (LW) emissivity, upward LW flux, deep snowpack treatment, and thermal conductivity of permanent ice and snow surfaces within the land surface model (LSM), as well as implementation of fractional sea-ice treatment specifying conditions associated with ice and open-water areas of sea-ice grid cells. These modifications improve model performance over the pan-Arctic for short-term forecasts, and Polar WRF ranks high among various model configurations in month-long simulations evaluating large-scale circulation and near-surface state variables [*Cassano et al.*, 2011].

[4] In the companion paper, state variables from Polar WRF short-term forecasts are evaluated during an annual cycle in preparation for ASR [*Wilson et al.*, 2011] (hereafter

---

[1]Polar Meteorology Group, Byrd Polar Research Center, Ohio State University, Columbus, Ohio, USA.
[2]Atmospheric Sciences Program, Department of Geography, Ohio State University, Columbus, Ohio, USA.
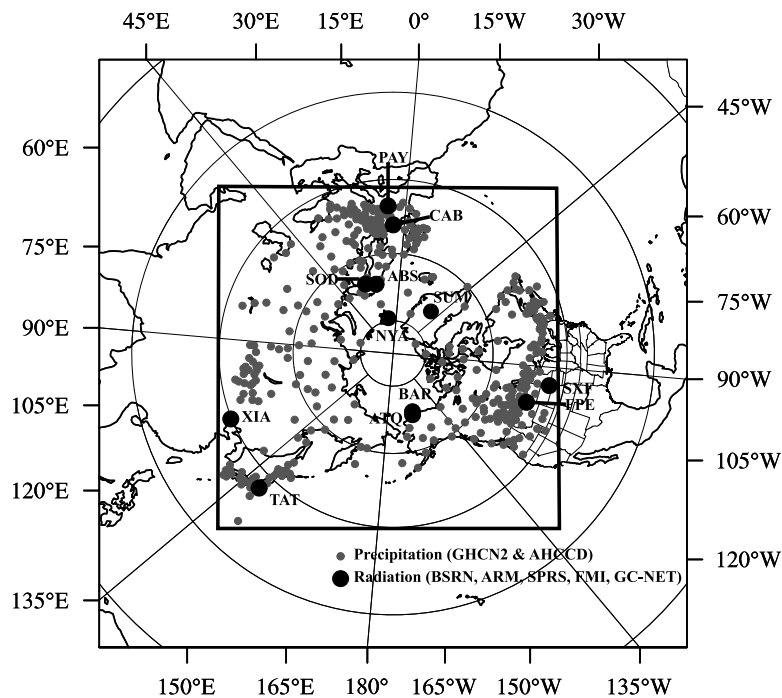
Figure 1. Two-way nested model domain used for Polar WRF simulations. Outer domain has 106×106 grid points with 180 km resolution and inner domain consists of 181×181 grid points with 60 km horizontal resolution. Small black dots represent precipitation sites (GHCN2 and AHCCD) used for precipitation comparison. Large black dots show the locations of sites used for radiation analysis. See Table 1 for abbreviations and site descriptions.

Part I). While Polar WRF simulates observed surface and upper air variables well, some model biases are discovered. First, a cold bias in the near-surface air temperature appears to be the result of the LSM. Despite the cold bias throughout most of the year, simulated 2 m dewpoint temperatures are higher than observed, especially in the midlatitudes. An evaluation of monthly evaporation for July shows Polar WRF overestimates evaporation compared to the European Centre for Medium-Range Weather Forecasts (ECMWF) 'Interim' reanalysis (ERA-Interim) [*Simmons et al.*, 2007] which leads to positive 2 m dewpoint temperature biases near the surface. Finally, Part I shows the near-surface diurnal 2 m temperature range is significantly larger in the model than observations. This appears to affect stability and near-surface winds, as well as imply a discrepancy in the model atmospheric opacity due to deficient cloud cover.

[5] With the results from Part I in mind, the focus of this paper is to analyze the forecast atmospheric hydrologic cycle and highlight deficiencies in model physics. Specifically, analysis is conducted on forecast precipitation, surface radiation, and clouds. The performance of the hydrologic cycle has received little evaluation in the course of Polar WRF development. Thus, to continue the preparation for the ASR, this study analyzes model results from the optimized Polar WRF model on the ASR domain. While this evaluation period deviates from the standard hydrological year (November 1 – October 31), the results are consistent with the evaluation period of Part I (December 2006 – November 2007). The paper is organized as follows. Section 2 describes the Polar WRF configuration and model domain used in this investigation. Section 3 describes the data sets

used for validation and methods employed to investigate clouds in the model. Section 4 details the precipitation analysis. Section 5 compares cloud observations to calculated cloud fraction (CF) from Polar WRF. Section 6 examines incident shortwave radiation (SW) and downwelling LW radiation at the surface for selected sites, and concluding remarks are provided in Section 7.

2. Polar WRF Configuration and Physics

[6] The annual simulation used in Part I to study the state variables is investigated in this study of the atmospheric hydrologic cycle with a brief description provided here. Polar WRF 3.1.1 is used with 39 vertical terrain-following sigma levels from the earth's surface to 10 hPa, with the lowest layer centered at 8 m AGL. "Forecast mode" is implemented with 48 h simulations initialized daily at 0000 UTC. This method allows model spin-up of the hydrologic cycle and the boundary layer and avoids errors that result over time despite updated lateral boundary conditions [*Lo et al.*, 2008]. Physics parameterizations for the full annual simulation have been chosen in light of previous Polar WRF experiments and include the WRF single moment 6-class microphysics scheme [*Hong and Lin*, 2006], the new Grell-Devenyi 3D ensemble cumulus scheme [*Skamarock et al.*, 2008], based on an older version [*Grell and Devenyi*, 2002], the Mellor-Yamada-Janjić boundary layer scheme (MYJ) [*Janjić*, 2002], the Rapid Radiative Transfer Model (RRTM) [*Mlawer et al.*, 1997] for LW radiation, and the Goddard SW scheme [*Chou and Suarez*, 1994] for SW radiation. Finally, the Noah Land Surface Model [*Chen and Dudhia*, 2001] with an Eta

similarity surface layer and fractional sea-ice are employed with a summer sea-ice albedo transition representing a mixed surface of bare ice and melt ponds (See Part I for a full description of the model parameterizations). Model results are output every 3 h and are aggregated for monthly and annual statistics where appropriate.

[7] The domain encompasses most of the Northern Hemisphere with a 2-way nested domain centered on the North Pole. The inner domain extends 10,800 km in the west-east and south-north directions on a 60 km horizontal grid (Figure 1). The inner domain boundaries are located inside the highest terrain of the Tibetan Plateau and capture the North Pacific and North Atlantic storm tracks and Arctic river drainage basins. The domain includes four key Arctic river basins (Ob, Lena, Yenisei, and Mackenzie) with sufficient station observations available within each basin for comparison with Polar WRF.

[8] The lateral boundary conditions are based upon the National Centers for Environmental Prediction (NCEP) Final global gridded analysis archive (National Centers for Environmental Prediction, NCEP FNL Operation Model Global Tropospheric Analyses, continuing from July 1999, Dataset ds083.2, 1999, updated daily, http://dss.ucar.edu/datasets/ds083.2./); a $1° \times 1°$ global grid updated every six hours. Sea surface temperatures are provided by the NCEP 0.5° RTG_SST Analysis [*Gemmill et al.*, 2007]. The sea-ice coverage is supplied by the Bootstrap Sea Ice Concentrations from the Defense Meteorological Satellite Program's (DMSP) Special Sensor Microwave/Imager (SSM/I) [*Comiso*, 1999] with 25 km resolution. Daily sea-surface temperature and sea-ice concentration are linearly interpolated to six hour inputs based on the difference between two consecutive days.

3. Data and Validation Methods

[9] Model precipitation is compared to observations from the Global Historical Climate Network (GHCN) version 2 [*Peterson and Vose*, 1997] and the Adjusted Historical Canadian Climate Data (AHCCD) [*Mekis and Hogg*, 1999]. As with Part I, the domain has been divided along 60 °N, with polar stations identified as stations north of this latitude. Three hourly model convective and non-convective precipitation totals are summed to model total precipitation which is then compared to monthly, seasonal, and annual precipitation observations. The GHCN2 data set has undergone a thorough quality control process [*Peterson and Easterling*, 1994; *Easterling and Peterson*, 1995]. This process includes a combination of regression analysis and non-parametric techniques in order to remove spurious mean and variance changes and to verify observations to climatology and neighboring stations spatially and in time. Several adjustments have been made to the AHCCD data to address wind under-catch, evaporation, as well as an adjustment for trace observations [*Mekis and Hopkinson*, 2004; *Mekis*, 2005; *Devine and Mekis*, 2008]. Only stations with a complete record for the annual cycle are included in this analysis (Figure 1).

[10] The ERA-Interim Reanalysis is used for a qualitative comparison of the spatial distribution of annual total precipitation as predicted by Polar WRF. The ERA-Interim data for this study are provided by the Data Support Section of the Computational and Information Systems Laboratory at the National Center for Atmospheric Research (NCAR). NCAR is supported by funding from the National Science Foundation. The original data are available from the Research Data Archive (http://dss.ucar.edu) in data set number ds627.0. In general, the annual cycle and spatial distribution of precipitation over land from ERA-Interim compare well with the Global Precipitation Climate Project (GPCP) [*Adler et al.*, 2003], and ERA-Interim is seen as an improvement over other reanalyses [*Trenberth et al.*, 2011]. However, Polar WRF is not verified directly against GPCP in this paper as this merged satellite-gauge product performs poorly in high latitudes when compared to gridded station observations [*Serreze et al.*, 2005]. Here, the output from ERA-Interim is on a $0.7° \times 0.7°$ Gaussian grid and has been projected onto the Polar WRF domain without interpolation. Annual precipitation totals are summed from twice daily 12 h forecast fields from ERA-Interim.

[11] Several observation data sets are used to compare CF, which is not a standard output from Polar WRF. It is computed based on the integrated cloud optical depth from the Community Climate Model 2 (CCM2) radiation scheme that is similarly used in Polar MM5 [*Hack et al.*, 1993]:

$$CF = C_1 * CLWP + C_2 * CIWP, \qquad (1)$$

where *CLWP* is the cloud liquid water path, *CIWP* is the cloud ice water path, and the weighting coefficients for C_1 and C_2 are 0.1 $m^2 g^{-1}$ and 0.0735 $m^2 g^{-1}$, respectively. The cloud ice and cloud water content affecting surface radiation have been shown in earlier studies to be important for estimating model-generated cloud cover [*Mölders et al.*, 1995, *Yarker et al.*, 2010]. *Fogt and Bromwich* [2008] use this formula but increase the CIWP coefficient in order to more accurately represent CF at McMurdo, Antarctica. *Hines et al.* [2011, Figure 10] show Polar WRF estimated CF using this formula compares well with observations in June and the beginning of July 2007 at Barrow, Alaska. It is not until later in July, as the pack ice pulls away from Barrow and a change in the local meteorology occurs that the model estimated CF differs greatly from the observed at this single location. It is interpreted that these derived CFs are accurate for homogeneous environmental conditions and are valid for the broad-scale comparisons conducted in this investigation. CF observations from the *National Climatic Data Center* (NCDC, see Figure 1 in Part I) are converted from octas to decimal values and compared to derived CFs from Polar WRF. This analysis focuses on July average cloud conditions as it pertains to other hydrologic variables examined.

[12] Cloud analysis is expanded to include cloud-derived products from the National Aeronautics and Space Administration's (NASA) Moderate Resolution Imaging Spectroradiometer (MODIS) aboard Terra and Aqua satellites as well as the collocated CloudSat radar and Cloud and Aerosol Lidar with Orthogonal Polarization (CALIOP) aboard the Cloud-Aerosol Lidar and Infrared Pathfinder Satellite Observations (CALIPSO) satellite. Recent improvements to cloud-detection schemes in MODIS are described by *Frey et al.* [2008] and *Ackerman et al.* [2008], where particular attention has been given to improving detection of clouds over land and ocean at night, during polar night, and over

Table 1. Radiation Measurement Sites

Station	Contacts and References	Instruments	Surface	Latitude, Longitude	Elevation (m)
Abisko, Sweden (ABS)	Annika Kristofferson Abisko Scientific Research Station *annika.kristofferson@ans.kiruna.se*	Kipp & Zonen Pyranometer, Eppley Pyrgeometer	Tundra/Flat, Rural	68° 21′ N, 18° 49′ E	385
Atqasuk, AK USA (ATQ)	Wanda Ferrell U.S. Department of Energy ARM Climate Research Facility Program Director *wanda.ferrell@science.doe.gov*	MFRSR	Tundra/Flat, Rural	70° 28′ N, 157° 24′ W	20
Barrow, AK USA (BAR)[a]	Ellsworth Dutton NOAA Barrow Climate Observatory *ellsworth.g.dutton@noaa.gov*	Eppley Pyranometer/ Pyrgeometer	Tundra/Flat, Rural	71° 19′ N, 156° 36′ W	11
Cabauw, The Netherlands (CAB)[a]	Fred Bosveld Royal Netherlands Meteorological Institute *fred.bosveld@knmi.nl*	Kipp & Zonen Pyranometer/ Pyrgeometer	Grass/Flat, Rural	51° 58′ N, 4° 56′ E	0
Fort Peck, MT USA (FPE)[a]	John Augustine Augustine *et al.* [2000] Augustine *et al.* [2005] *john.a.augustine@noaa.gov*	Spectrosun Pyranometer, Eppley Pyrgeometer	Grass/Flat, Rural	48° 19′ N, 105° 06′ W	634
Payerne, Switzerland (PAY)[a]	Laurent Vuilleumier *laurent.vuilleumier@meteoswiss.ch*	Kipp & Zonen Pyranometer, Eppley Pyrgeometer	Cultivated/Hilly, Rural	46° 49′ N, 06° 57′ E	491
Ny-Ålesund, Svalbard (NYA)[a]	Marion Maturilli *marion.maturilli@awi.de*	Kipp & Zonen Pyranometer, Eppley Pyrgeometer	Tundra/Mountain Valley, Rural	78° 55′ N, 11° 55′ E	11
Sioux Falls, SD USA (SXF)[a]	John Augustine Augustine *et al.* [2000] Augustine *et al.* [2005] *john.a.augustine@noaa.gov*	Spectrosun Pyranometer, Eppley Pyrgeometer	Grass/Hilly, Rural	43° 44′ N, 96° 37′ W	473
Sondankylä, Finland (SOD)	Reija Ruuhela Finnish Meteorological Institute *reija.ruuhela@fmi.fi*	Kipp & Zohen Pyranometer	Boreal/Hilly, Rural	67° 22′ N, 26° 39′ E	180
Summit, Greenland (SUM)	Konrad Steffen Steffen *et al.* [1996] *konrad.steffen@colorado.edu*	Li Cor Photodiode	Flat/Ice Sheet	72° 35′ N, 38° 30′ W	3254
Tateno, Japan (TAT)[a]	Nozomu Ohkawara Aerological Observatory Japan Meteorological Agency *ohkawara@met.kishou.go.jp*	Kipp & Zonen Pyranometer, Eppley Pyrgeometer	Grass/Flat, Rural	36° 03′ N, 140° 08′ E	25
Xianghe, China (XIA)[a]	Xiangao Xia *xiangaoxia2000@yahoo.com*	Kipp & Zonen Pyranometer, Eppley Pyrgeometer	Desert, Rock/Flat, Rural	39° 45′ N, 116° 58′ E	32

[a]Data for these sites are obtained through the Baseline Surface Radiation Network (BSRN) [*Ohmura et al.*, 1998]. All other station information is provided through personal contact with the leads indicated under Contacts and References. The abbreviations are in parentheses for each station, and they are used consistently throughout the paper.

snow and ice surfaces during the day. CloudSat radar and CALIPSO lidar, each with its own sensitivities to different cloud types, have been combined to analyze clouds [*Mace et al.*, 2009] and produce gridded monthly CF [*Kay and Gettelman*, 2009]. The lidar, such as the one aboard CALIPSO, allows for better detection of polar clouds than passive infrared such as MODIS since it is based on an active signal return and not thermal differences of surfaces. However, MODIS has greater spatial and temporal coverage scanning the entire globe every one to two days whereas the active lidar signal on CALIPSO is restricted to a 100 m wide footprint along the orbital track of the satellite. For this reason, MODIS CF is thought to represent the most accurate observed CF as it relates to the percentage of sky in fact covered by clouds.

[13] Finally, radiation measurements from a number of sources have been collected for this analysis (Table 1). Data for Abisko, Sweden has been provided by Annika Kristofferson of Swedish Polar Research Secretariat (SPRS) Abisko Scientific Research Station (http://www.linnea.com/ ~ans/). Measurements for Atqasuk, Alaska have been obtained through the Atmospheric Radiation Measurement (ARM) [*Ackerman and Stokes*, 2003] North Slope of Alaska (NSA) site which includes multifilter rotating shadowband radiometer (MFRSR) downwelling SW flux, "best estimate" broadband downwelling SW flux (both diffuse and direct), and broadband downwelling LW flux. Incident SW radiation data for Sodankylä, Finland has been provided by Reija Ruuhela of the Climate Service Centre of the Finnish Meteorological Institute and for Summit, Greenland through the Greenland Climate Network [GC-Net; http://cires. colorado.edu/science/groups/steffen/gcnet/]. Finally, data for the remaining stations originate from the World Climate Research Program Baseline Surface Radiation Network
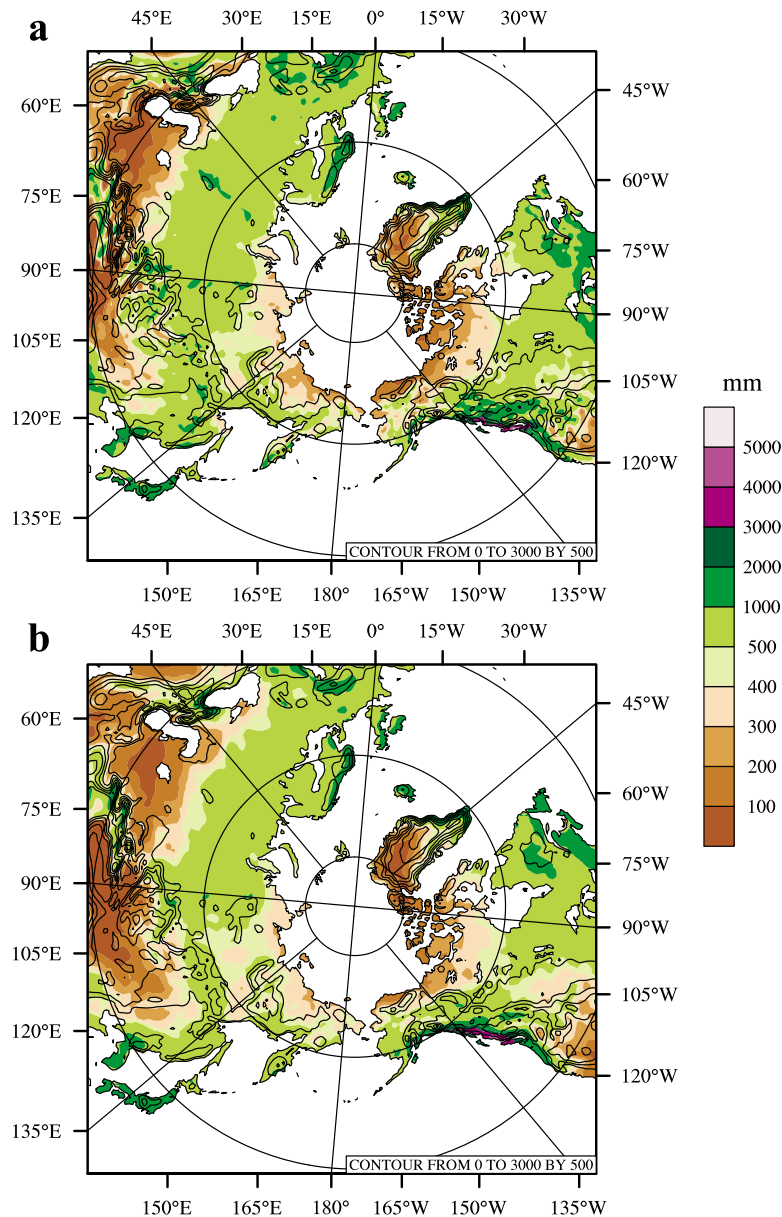
Figure 2. Annual total precipitation (mm) over land for December 2006 – November 2007 for (a) Polar WRF and (b) ERA-Interim. ERA-Interim 0.7° × 0.7° data have not been re-gridded to Polar WRF resolution. Terrain elevation is contoured from 0 m to 3000 m in 500 m increments. Color scale is nonlinear.

[*Hegner et al.*, 1998; *Ohmura et al.*, 1998]. Figure 1 shows the locations of the radiation sites used in this analysis.

4. Precipitation

4.1. Spatial Precipitation Analysis

[14] Polar WRF spatial patterns of annual total precipitation match well with ERA-Interim (Figure 2). Overall, the wettest conditions are located throughout the midlatitudes and the southern sub-polar regions of Canada and Russia in the predominant storm-track regions. Simulated annual precipitation greater than 1000 mm can be found from southern Alaska through British Columbia and into the northwest United States, along the steep terrain in southeast Greenland, South Korea and Japan, and in the humid continental region

east of the Black Sea where higher elevation leads to increased vertical lift and precipitation rates. High precipitation along the steep terrain in Greenland due to the North Atlantic storm track has been shown in previous mesoscale modeling studies with Polar MM5 predicted totals for 1997–1998 exceeding 4000 mm yr^{-1} [*Cassano et al.*, 2001]. Polar WRF precipitation agrees spatially well with this finding, where the highest annual totals for Greenland (1000–3000 mm yr^{-1}) are demonstrated in the same region. Another area of interest is the west coast of North America where high precipitation totals (some exceeding 5000 mm yr^{-1}) are predicted by Polar WRF and are similarly reflected by the ERA-Interim Reanalysis. This phenomenon has been previously identified in modeling studies of MM5 [*Colle et al.*, 1999], who show

Table 2. Annual, Seasonal, and Monthly Precipitation Biases[a]

	Ann	Win	Spr	Sum	Aut	Dec	Jan	Feb	Mar	Apr	May	Jun	Jul	Aug	Sep	Oct	Nov
						Midlatitude N = 305											
PWRF	854.3	158.6	194.8	323.1	177.8	52.7	55.1	50.8	58.3	49.0	87.5	113.7	114.5	94.9	69.2	52.5	56.1
OBS	817.0	172.0	173.8	265.0	206.2	60.3	61.2	50.5	57.3	39.8	76.7	84.1	98.5	82.4	80.2	61.6	64.4
BIAS	37.3	−13.4	21.0	58.1	−28.4	−7.6	−6.1	0.3	1.0	9.2	10.8	29.6	16.0	12.5	−11.0	−9.1	−8.3
						Midlatitude (North America) N = 128											
PWRF	812.4	149.6	211.9	275.8	171.0	52.8	48.0	48.8	64.7	70.6	80.7	101.2	98.0	76.6	58.0	58.4	54.6
OBS	735.8	150.5	174.1	218.1	193.2	53.8	50.7	46.0	57.8	51.2	65.1	80.7	66.5	70.9	65.7	65.2	62.3
BIAS	76.6	−0.9	37.8	57.7	−22.2	−1.0	−2.7	2.8	6.9	19.4	15.6	20.5	31.5	5.7	−7.7	−6.8	−7.7
						Midlatitude (Western Europe) N = 94											
PWRF	952.0	197.8	201.2	383.3	171.5	53.5	81.4	62.8	60.2	26.0	113.1	151.6	116.7	115.0	66.8	40.4	64.4
OBS	880.6	212.7	172.0	292.1	203.9	61.0	86.2	65.4	62.3	16.3	93.3	93.9	104.2	93.9	81.8	44.9	77.2
BIAS	71.4	−14.9	29.2	91.2	−32.4	−7.5	−4.8	−2.6	−2.1	9.7	19.8	57.7	12.5	21.1	−15.0	−4.5	−12.8
						Midlatitude (Asian) N = 40											
PWRF	651.6	63.4	166.1	348.0	125.9	22.5	15.8	25.2	30.8	30.7	52.8	97.1	146.3	104.6	65.8	38.1	21.9
OBS	549.8	60.5	104.0	288.8	96.5	22.6	16.9	21.1	26.6	28.0	49.4	64.7	130.4	93.7	48.0	32.4	16.1
BIAS	101.8	2.9	62.1	59.2	29.4	−0.1	−1.1	4.1	4.2	2.7	3.4	32.4	15.9	10.9	17.8	5.7	5.8
						Polar N = 78											
PWRF	564.6	120.9	111.9	171.5	160.3	48.5	46.9	25.5	35.7	34.9	41.3	43.0	69.5	59.0	59.9	53.5	46.9
OBS	623.4	132.7	123.3	185.1	182.3	53.1	51.8	27.8	39.5	37.0	46.8	50.5	62.6	72.0	67.0	56.6	58.7
BIAS	−58.8	−11.8	−11.4	−13.6	−22.0	−4.6	−4.9	−2.3	−3.8	−2.1	−5.5	−7.5	6.9	−13.0	−7.1	−3.1	−11.8

[a]All precipitation totals and biases are in mm. Midlatitude stations are those lying south of 60 °N while Polar stations are those north of this latitude. N is the number of station included in each domain. Ann, annual; Win, winter; Spr, spring; Sum, summer, Aut, autumn.

excessive precipitation along the windward slopes of the Cascade Mountains.

[15] Areas of lighter annual precipitation spatially agree with ERA-Interim as well. The Arctic, northern Greenland, and the tundra regions of northern Canada and Siberia show dry conditions (less than 300 mm of annual precipitation) representative of the long cold winters in these areas. The Caspian Sea region and the Tibetan Plateau reflect the dry influence of subtropical high pressure at these latitudes, where less than 100 mm of annual precipitation falls.

### 4.2. Observational Analysis of Annual, Seasonal, and Monthly Precipitation

[16] Polar WRF annual, seasonal, and monthly precipitation biases for the midlatitude and polar regions have been calculated for 305 and 78 stations, respectively (Table 2). Likewise, biases for three regional clusters of available sites throughout North America (South of 60°N, 135°W – 45°W), Western Europe (South of 60°N, 15°W – 45°E), and Asia (South of 60°N, 90°E – 135°E), are calculated and shown in Table 2 as well. The midlatitude mean annual bias is 37.3 mm (4.6%), reflecting a wetter prediction in annual precipitation for this region. The polar region has a negative bias of −58.8 mm (−9.4%), strongly affected by stations along the NSA and in the Canadian Archipelago.

[17] Figure 3 shows the annual precipitation biases in total (mm) and percentage error between the model and observations. For midlatitude annual precipitation, 62% of all station biases are within ±50% of observed totals (35% within ±25%), while 69% of polar station biases are within ±50% (44% within ±25%). Despite the relatively small midlatitude annual mean bias, there are few stations within ±5% of the observed total indicating the model substantially over/underpredicts precipitation in this region. In fact, only 28 midlatitude and 7 polar station annual biases are not significant at 95% confidence based on 12 monthly

precipitation totals. Several distinct regions of positive annual precipitation bias in the midlatitudes including central and eastern Canada, Europe, and higher elevations in Asia are reflected. For the Asia region, the positive biases exist throughout the entire annual cycle. Coupled with stations along the Rockies, particularly the rain shadow areas to the east, this overprediction appears to be the result of 60 km resolution where the effects of high terrain are not well captured. Too much moisture remains on the lee side of the highest elevations in the model leading to excess precipitation in these regions. Smoothed terrain in the model also results in a juxtaposition of positive and negative biases, assuming the small scale effects on precipitation (local wind circulations) are not captured with precision. Another area of positive precipitation biases are along the windward sides of steep terrain, particularly along the west coast of North America. While agreeing spatially with ERA-Interim, these large positive biases are greater than 25% of observed and suggest increased moisture due to moisture transport off the North Pacific. Studies have shown a large difference in the amount of precipitation between coastal sites in this region and precipitation in the higher elevations just to the east due to orographic enhancement [e.g., *Neiman et al.*, 2002; *White et al.*, 2003]. With 60 km resolution, the model grid points used to compare with observations are influenced by this orographic precipitation and an overprediction of precipitation appears.

[18] As mentioned in the previous section, areas along the coast of Japan, the United Kingdom, and stations throughout the Canadian archipelago reflect dry biases. For stations along the western coast of Scandinavia with underpredicted annual precipitation, precipitation is typically enhanced by orographic lift and local wind effects throughout the valleys of the fjords [*Barstad et al.*, 2009] which may be difficult to capture at 60 km horizontal resolution. The Canadian
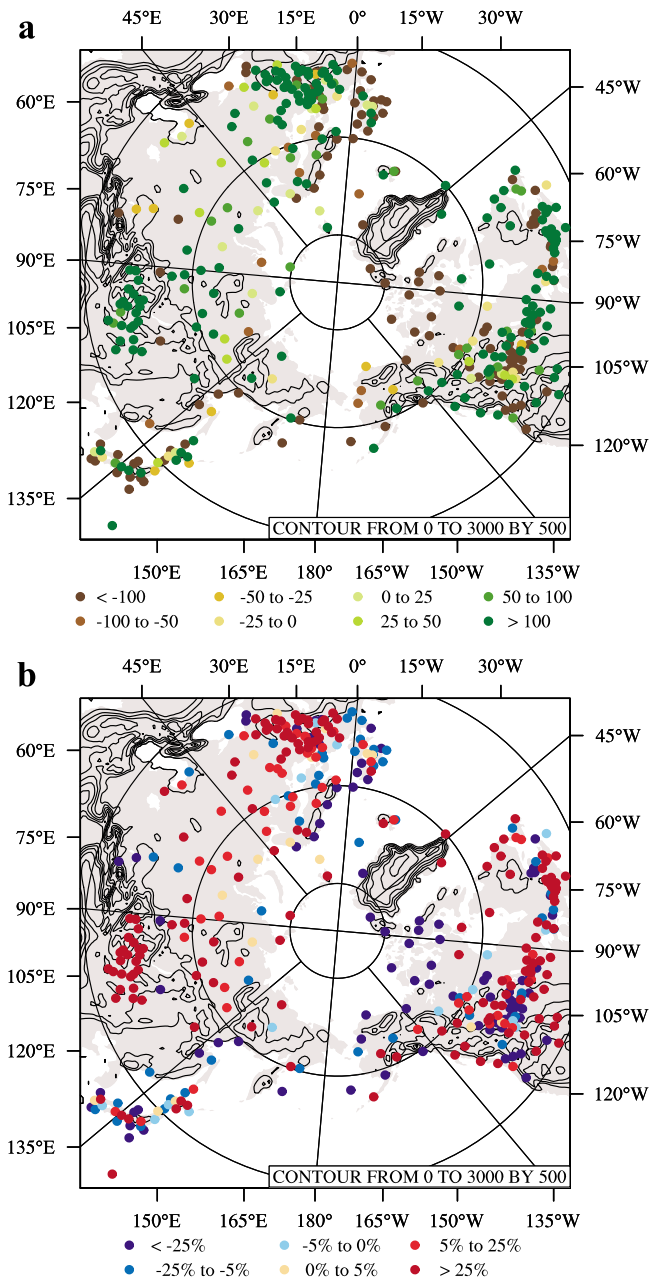
Figure 3. (a) Annual total precipitation biases (mm) and (b) percent biases (%) compared to surface observations from GHCN2 and AHCCD. Terrain elevation is contoured from 0 m to 3000 m in 500 m increments.

Archipelago, which is made up of several islands, shows dry biases throughout the entire year (not shown). *Serreze et al.* [1995] determined the Canadian Archipelago to be an area of annual mean equatorward water-vapor transport due to northwesterly geostrophic wind influence. An investigation of the meridional wind in Part I, however, shows strong southerly wind biases in this region which may be limiting the amount of water vapor available for precipitation.

[19] Seasonal differences between model and observed precipitation totals range from −28.4 mm to +58.1 mm in the midlatitudes and −22.0 mm to −11.4 mm in the polar region (Table 2). These seasonal differences reveal a discrepancy between midlatitude warm and cool season precipitation regimes. Figure 4 shows monthly Polar WRF and observed precipitation totals, biases, and Polar WRF convective and non-convective precipitation. In the midlatitudes, February and March precipitation biases are small, +0.5% and +1.7% respectively. From spring into summer, large positive precipitation biases occur, especially in June (+35.2%), July (+16.2%), and August (+15.2%). In the polar region, negative precipitation biases range from −20.1% to −5.5% in all months except July (+11.0%) when the greatest contribution to model precipitation is convective. During months with negative biases, the precipitation is the result of primarily synoptically driven weather patterns and less from convection. However, in July several stations (near or just north 60 °N) experience large precipitation biases and increased convective precipitation supporting the notion that excessive convection in the warm months leads to an over-prediction of precipitation in the model.

[20] To understand the reason for this increased convective precipitation in the model, several sensitivity simulations are performed for July 2007 and the results are shown in Figure 5. First, the microphysics parameterization is changed to the Morrison double-moment scheme [*Morrison et al.*, 2009; *Morrison and Pinto*, 2006; *Morrison et al.*, 2005]. This scheme has proven to be successful in Polar WRF Arctic applications [*Bromwich et al.*, 2009; *Hines et al.*, 2011]. Next, the cumulus parameterization is tested using the modified Kain-Fritsch scheme [*Kain*, 2004; *Kain and Fritsch*, 1993, 1990]. For both the microphysics (MORR) and cumulus parameterization (KAIN) changes, the overprediction of July precipitation is still present, with little change in the non-convective and convective components. A final sensitivity simulation is performed using a grid-nudging technique where the model is nudged toward analysis interpolated in time and space in order to improve topographic and convective effects [*Skamarock et al.*, 2008; *Stauffer and Seaman*, 1990]. Here, specific humidity is nudged in the boundary layer with temperature and winds being left un-nudged (QVAPOR). Figure 5 shows the July precipitation total has decreased by approximately 25% for the nudged run and is now reflecting a negative bias. More importantly, a large decrease in the convective component is discovered. A time series of the specific humidity for individual grid points shows that at each time the model is nudged, the specific humidity near the surface is nudged toward a drier value. This test indicates the model boundary layer specific humidity is too high, which leads to increased moisture available for processes such as convection.

[21] Increased lower tropospheric moisture is also supported in Part I where the 2 m dewpoint temperatures in July 2007 are overpredicted, lower tropospheric relative humidity is high, and evaporation compared to ERA-Interim is excessive. Another potential source of error includes biased soil moisture conditions. *Hines et al.* [2011] show that evaporation increases when soil moisture is increased in the upper soil layers. Although there is little impact on the cloud radiative fields, biased soil moisture conditions could lead to increased evaporation and more moisture available for precipitation. Therefore, as ASR is undertaken, it is hypothesized the use of atmospheric data assimilation, land-surface data assimilation, and advances in boundary layer schemes will
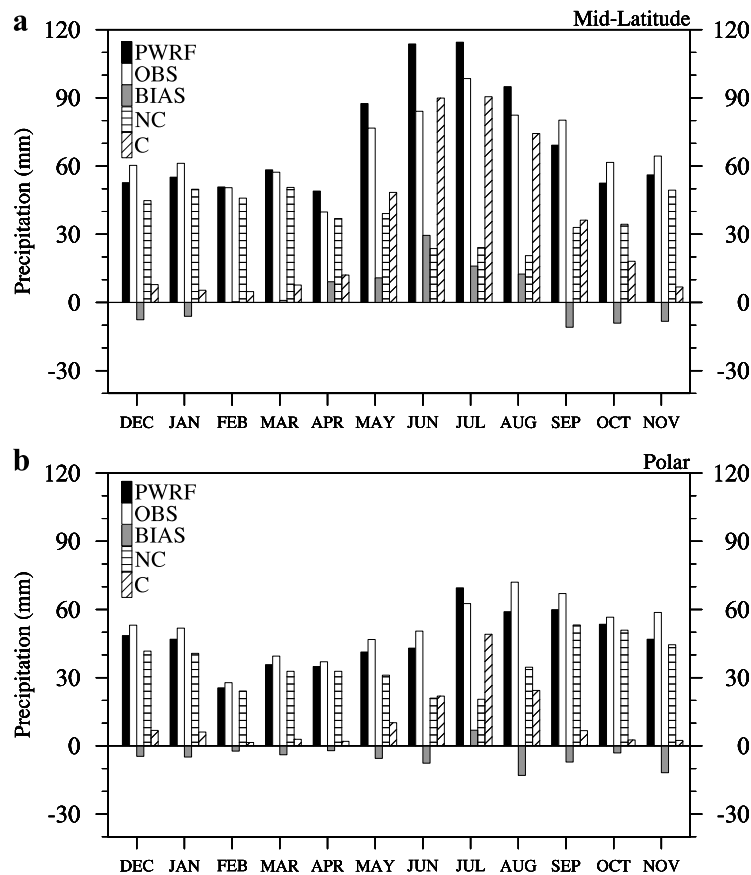
Figure 4. Monthly precipitation totals (mm) for Polar WRF and observations for (top) midlatitude and (bottom) polar region. The bias (gray) is the monthly model precipitation minus monthly observed precipitation. Non-convective (NC, horizontal lines) and convective (C, diagonal lines) components of the monthly model precipitation totals are also provided.

improve the analyzed moisture conditions and avoid the excessive convective precipitation revealed in this investigation.

### 4.3. Arctic River Basin Precipitation Analysis

[22] Model precipitation bias has an implication on the freshwater supply to the Arctic Ocean through the drainage of four major river basins (Figure 6; Ob, Yenisei, Lena, and Mackenzie). The headwaters of these rivers begin as far south as 45 °N (Yenisei in Northern Mongolia), demonstrating the strong link between midlatitude atmospheric processes and their effects on the Arctic. This freshwater runoff into the Arctic Ocean is vital to the Arctic climate system including Northern Hemisphere sea ice as well as global ocean circulation.

[23] Annual and seasonal precipitation totals and biases for model grid point locations and observations within each of these river basins have been calculated (Table 3). The three river basins in Russia reflect an overprediction of precipitation by Polar WRF consistent with Figure 4. The Yenisei River region shows the largest positive annual bias of 204.4 mm (+57.5%), which is significant at the 99% confidence level. In fact, precipitation biases for all of the Russian rivers are highest in spring and summer. Model results for the Mackenzie River basin show the smallest yet
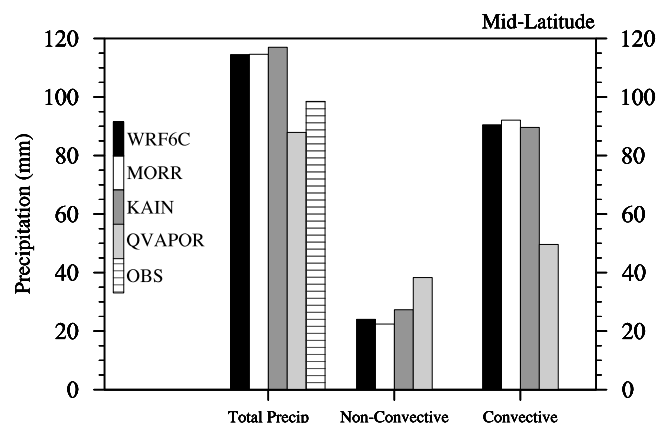
Figure 5. July 2007 total midlatitude precipitation (mm) for Polar WRF control simulation (black), Morrison double-moment microphysics scheme simulation (white), Kain-Fritsch cumulus scheme simulation (dark gray), and QVapor nudged simulation (light gray), and Observations (white/horizontal bar). Model-only non-convective and convective precipitation components (mm) included for all simulations.
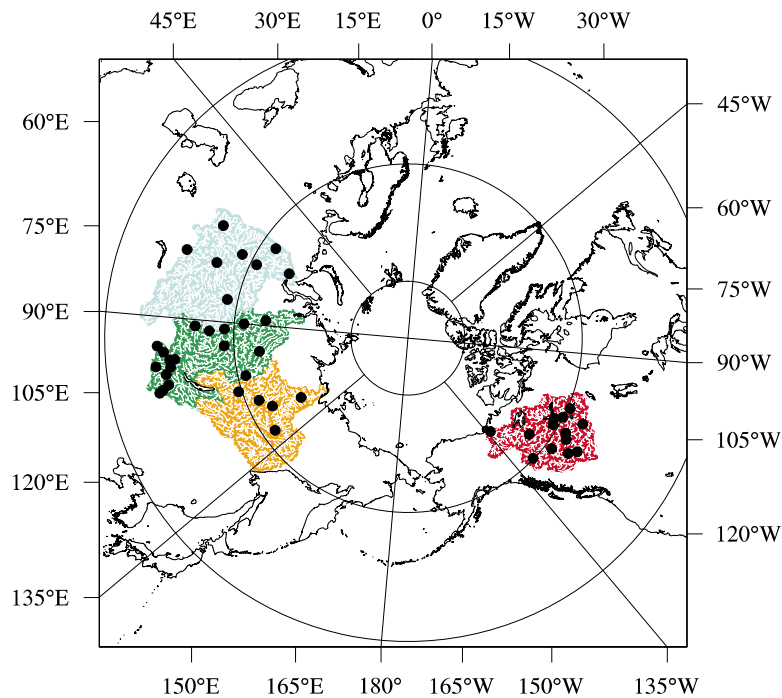
Figure 6. The major river basins of the Arctic (Ob-light blue, Yenisei-green, Lena-orange, and Mackenzie-red). Streams and rivers plotted within each basin are provided by the USGS (http://eros.usgs.gov/#/Find_Data/Products_and_Data_Available/gtopo30/hydro/) and stations used for basin precipitation statistics are noted (black dots). Arctic river basin data provided by Arctic-RIMS (http://rims.unh.edu/).

negative annual bias. Given the location of the Mackenzie River just to the east of the Mackenzie Mountains, precipitation predictions here as with other higher terrain locations may be hindered by model resolution and smoothed terrain.

[24] Monthly model and observed precipitation totals, biases, and model non-convective and convective contributions for each month for all four rivers are provided in Figure 7. It is apparent that greatest precipitation falls in the warm season months in all four river basins. However, the peak in precipitation ranges from June to August. For the Russian rivers, excessive convection is contributing to the large positive biases during the warm months, as supported by the number of stations with significant differences between the model and observed precipitation. Overall, seasonal precipitation totals in all river basins show Polar WRF correlating well in time for the four river basins (r² values ranging from 0.97 to 0.99), suggesting Polar WRF is appropriately representing the precipitation cycle throughout the year.

[25] Unlike the precipitation biases for the Russian rivers, there are large positive and negative biases from late spring though summer in the Mackenzie River basin. Additionally, the May and June negative biases are seen in all but one station included in the Mackenzie River regional mean for each month. It is hypothesized that these errors are occurring as a result of the influence of the overall wind flow. Polar WRF is overpredicting the simulated zonal component of the wind aloft in this region (see Part I), limiting the meridional wind influence. Precipitation in the southern extent of the Mackenzie River basin is affected by the Great Plains low level jet, as it transports moisture from the Gulf of Mexico

northward and lee cyclogenesis occurs in Alberta, Canada [*Brimelow and Reuter*, 2008]. This process results in extreme precipitation events for this region, with records indicating more than 100 mm for individual events. The maximum monthly recorded total precipitation for June 2007 at a single station in this basin is 171.2 mm while Polar WRF simulated 112.3 mm for the same station. These single extreme events may not be modeled precisely by Polar WRF

Table 3. Annual and Seasonal Precipitation Biases: Arctic Rivers[a]

	Ob N = 8			Yenisei N = 18		
	PWRF	OBS	BIAS	PWRF	OBS	BIAS
Annual	620.8	529.9	80.9	559.6	355.2	**204.4**
Winter	107.5	99.6	7.9	50.8	38.9	11.9
Spring	146.9	117.0	*29.9*	101.3	54.9	**46.4**
Summer	289.1	215.3	*73.8*	310.0	187.7	**122.3**
Autumn	77.2	98.0	−20.8	97.5	73.7	23.8

	Lena N = 5			Mackenzie N = 13		
	PWRF	OBS	BIAS	PWRF	OBS	BIAS
Annual	478.4	385.0	93.4	496.3	525.8	−29.5
Winter	60.6	53.0	7.6	71.9	75.7	−3.8
Spring	90.5	45.6	*44.9*	125.6	125.1	0.5
Summer	198.2	173.6	24.6	187.7	197.1	−9.4
Autumn	129.1	112.8	16.3	111.1	127.9	−16.8

[a]Annual and seasonal precipitation totals (mm) for Polar WRF (PWRF) and Observations (OBS) and biases (BIAS, mm) for the Ob River, the Yenisei River, the Lena River, and the Mackenzie River. Indices that are italicized boldface indicate annual and seasonal means are statistically significant at 90% confidence level, just italicized for 95%, and just boldfaced for 99%.
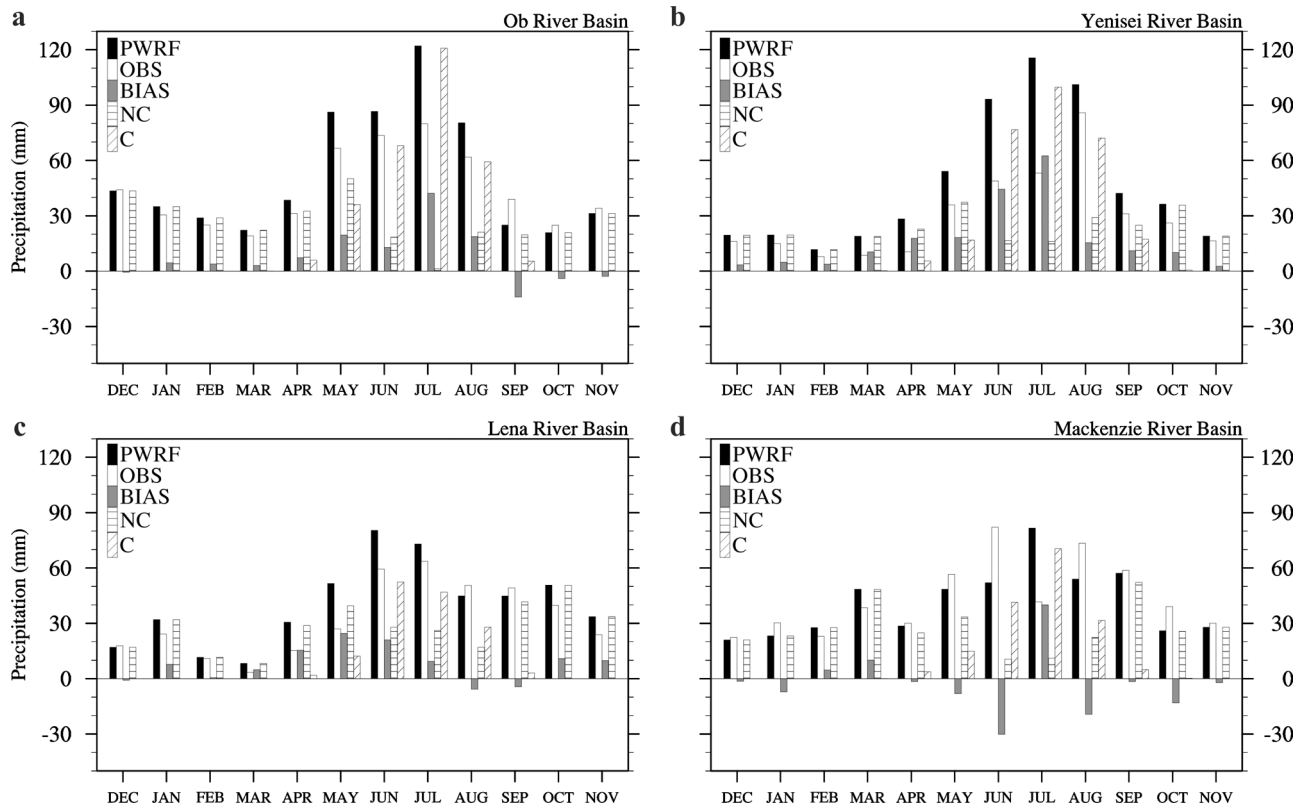
Figure 7. Monthly precipitation totals (mm) for Polar WRF and observations for the (a) Ob River Basin, (b) Yenisei River Basin, (c) Lena River Basin, and (d) Mackenzie River Basin. The bias (gray) is the monthly model precipitation minus monthly observed precipitation. Non-convective (NC, horizontal lines) and convective (C, diagonal lines) components of the monthly model precipitation totals are also provided.

leading to the large negative precipitation biases, although this is merely hypothesis since the precipitation data used in this study are monthly precipitation totals. By July, the convective precipitation bias previously discussed leads to a large overprediction in precipitation in the Mackenzie River region during this month, which is not enough to counter the negative biases in June and August resulting in a negative summer season bias.

5. Clouds

[26] Although cloud observations from trained weather observers are assumed to have associated error, qualitative cloud conditions from NCDC observations are converted to the following decimal values ranges: clear sky ($0 \leq CF \leq 0.125$), scattered ($0.125 < CF \leq 0.5$), broken ($0.5 < CF \leq 0.875$, and overcast ($CF > 0.875$). Both the model (equation (1)) and observed CF are compared every 3 h for January and July, and a percentage of occurrences are calculated for each of the above categories. Next, each category percentage of occurrences for the model and observed is multiplied by the average decimal value representing each category (0.0625, 0.3125, 0.6875, and 0.9375, respectively). The sum of the four categories is an indicator of cloudiness for the model and observations. Biases and percentage differences are calculated for 273 stations in January 2007 and

268 stations in July 2007 and are shown in Figure 8. Similar to the terrain resolution issues imposed on the precipitation analysis in areas of high terrain, the CF analysis reveals the same difficulty in accurately predicting clouds in these areas due to fine-scale local wind circulations. For January, a few stations show positive CF biases including western Europe and the coastal stations in western North America. This is consistent with strong 850 hPa zonal flow and advection of moisture from the North Atlantic and North Pacific. Overall, CF biases are small throughout most of Europe, midlatitude Asia, and northern and eastern Canada where bias percentage errors are within ±25%. For July, a majority of stations in the domain reflect negative CF biases compared to observations, which can have a substantial impact on near-surface variables. Lower CF in the summer infers increased incident SW radiation reaching the surface during the day (warmer temperatures, increased evaporation) and less cloud cover at night leads to less downwelling LW radiation with increased radiational cooling as seen in the diurnal temperature plots discussed in Part I. The bias percentage errors increase in July, with a majority of the station biases throughout the domain reflecting negative biases greater than 25%. The impact of cloud deficit on SW and LW radiation is directly shown in Section 6.

[27] To support the surface observations of cloud cover, monthly average CF for July 2007 is calculated and plotted
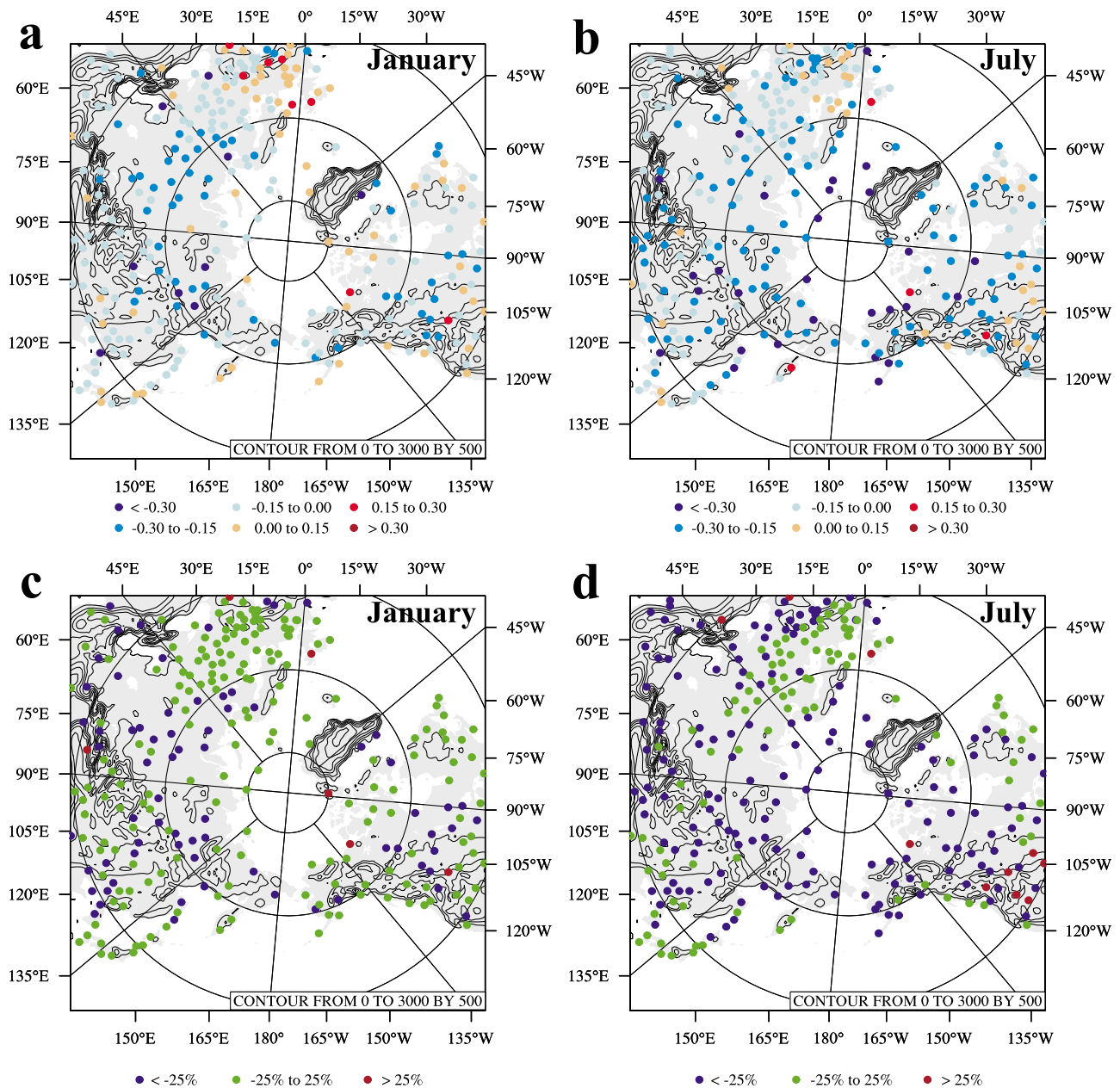
Figure 8. CF biases based on NCDC converted cloud conditions for (a) January 2007 and (b) July 2007. Percentages of cloud fraction biases for (c) January 2007 and (d) July 2007. Terrain elevation is contoured from 0 m to 3000 m in 500 m increments.

in Figure 9. Polar WRF CF based on the vertically integrated cloud liquid water and cloud ice is computed and averaged for all 3 h model output for July 2007 (Figure 9a). A cloud frequency (CFreq) is defined by the ratio of the 3 h forecasts when the model CF exceeds zero to the total number of forecasts (248) for July 2007 (Figure 9b), the same method used by *Nicolas and Bromwich* [2011] to examine clouds in Antarctic modeling. This approach represents a conservative method, providing the model the best chance of having clouds at each grid point. CF from MODIS is derived from the cloud mask probabilities and is provided as a Level 3 product [*Hubanks et al.*, 2008] (http://modis.gsfc.nasa.gov/). The MODIS cloud mask estimates the probability that a 1 km^2 pixel is cloudy or clear. The average CF within a 5 ×

5 km grid cell is calculated as the fraction of 1 km^2 pixels that are marked cloudy. The final cloud mask CF is an average of the 5 × 5 km cloud fractions within a 1° × 1° grid cell (Figure 9c). Finally, the gridded monthly CF from CloudSat/CALIPSO [*Kay and Gettelman*, 2009], represented by the CFreq or ratio of cloud detection from the merged cloud mask products over a 2° × 2° grid cell for July 2007 is shown in Figure 9d. It should be noted however, the gridded monthly CF for CloudSat/CALIPSO is limited by reduced temporal and spatial sampling, especially in areas farthest from the pole.

[28] Polar WRF shows greater CFs in areas of higher terrain, most likely associated with orographic lift and positive precipitation biases described in Section 4. Greater CF can
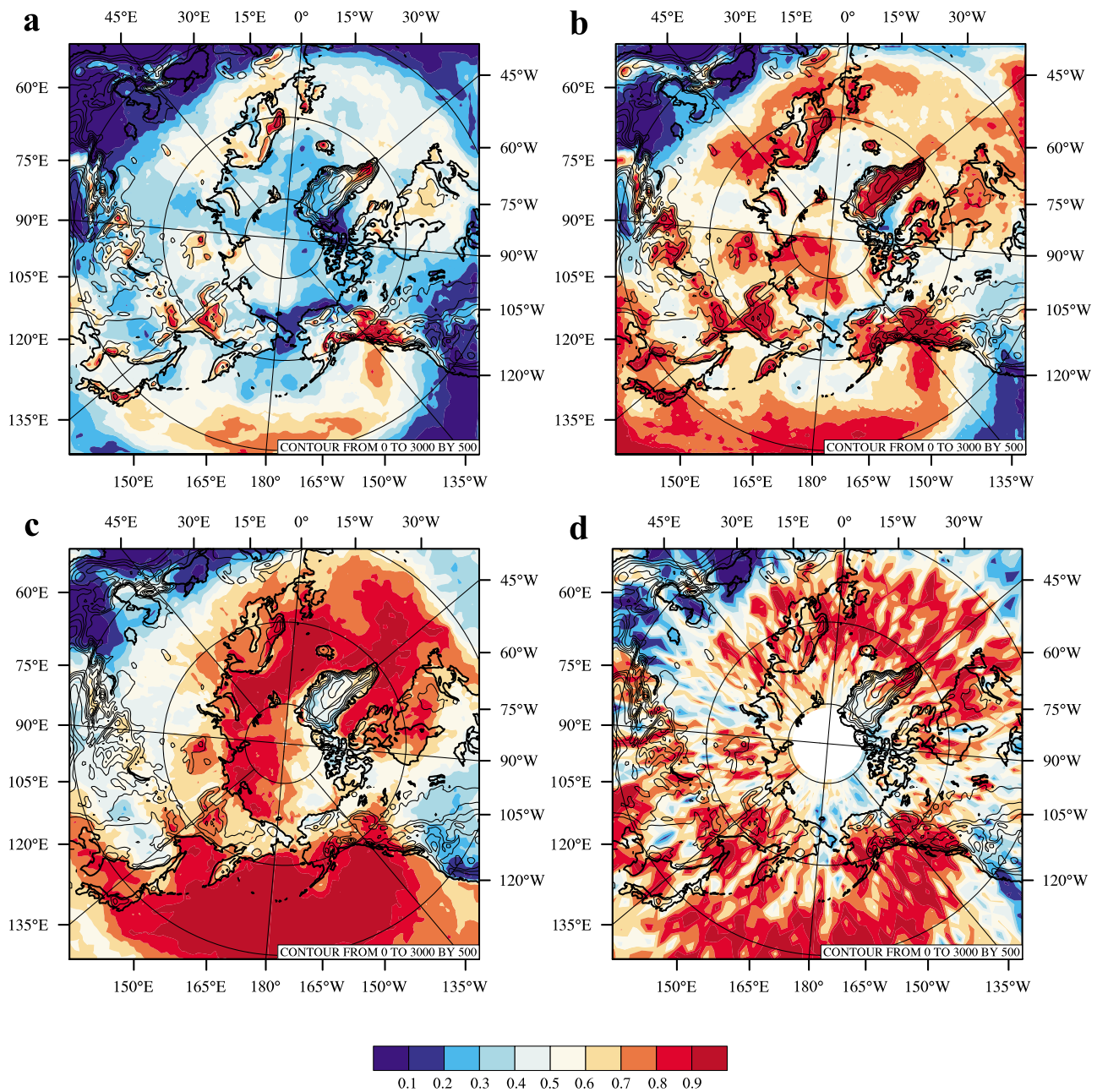
Figure 9. July 2007 (a) Polar WRF computed monthly average CF based on vertically integrated cloud water and cloud ice, (b) Polar WRF CFreq defined by the ratio of the 3 h forecasts where the model CF exceeds zero to the total number of forecasts (248) for July 2007, (c) MODIS CF based on the cloud mask estimates of cloudy 1 km² pixels averaged within a 5 × 5 km grid cell on a 1° × 1° grid, and (d) CloudSat/CALIPSO based on the merged cloud mask product on a 2° × 2° grid . Terrain elevation is contoured from 0 m to 3000 m in 500 m increments.

also be found along the North Pacific and North Atlantic storm tracks, although less than depicted by MODIS. In a limited area Polar WRF simulation along the NSA, *Hines et al.* [2011] show that increasing late spring and summer model CFs at Barrow, Alaska are consistent with observations [*Wendler and Eaton*, 1990; *Walsh et al.*, 2009]. Although *Kay et al.* [2008] note that 2007 was a particularly cloud free summer especially in the western Arctic, CF of 0.1 to 0.2 found in this study for the land in the

western Arctic is even lower than CF discovered by *Hines et al.* [2011]. Likewise, there is no apparent increase in cloudiness over the adjacent Arctic Ocean where summertime cloud cover often consists of multiple stratus layers [*Curry et al.*, 1996]. CF over the entire Arctic Ocean remains much lower than observed by MODIS, suggesting an underrepresentation of Arctic stratus clouds in the model.

[29] Figure 9b shows the alternate CFreq method. Since calculated CF greater than zero is counted toward the CFreq,

Table 4. Seasonal SW and LW Radiation Biases[a]

| Name | LW W m^{-2} | | | | | SW W m^{-2} | | | | |
	OBS	BIAS	RMSE	r	NUM	OBS	BIAS	RMSE	r	NUM
					January 2007					
ABS	221.1	**-47.1**	55.2	0.57	248	1.3	−0.1	2.5	0.86	248
ATQ	188.9	**-44.5**	52.0	0.67	243	1.1	**-1.0**	1.9	0.43	248
BAR	183.3	**-39.7**	49.5	0.45	244	0.1	**-0.1**	0.7	0.26	248
CAB	315.0	**-60.5**	66.3	0.80	248	25.7	5.5	36.9	0.85	248
FPE	225.4	**-30.5**	41.2	0.72	248	65.0	17.3	45.2	0.96	247
PAY	294.2	**-62.8**	70.9	0.60	248	51.3	−9.9	72.6	0.71	248
SOD	NA	NA	NA	NA	NA	2.5	0.2	6.5	0.70	248
SUM	NA	NA	NA	NA	NA	0.13	**-0.13**	0.50	NA	248
SXF	202.2	**-25.8**	40.7	0.65	248	85.0	**25.2**	57.2	0.96	248
TAT	270.6	**-34.8**	44.7	0.54	248	115.8	*29.8*	74.3	0.95	248
XIA	210.6	**-15.6**	23.9	0.56	248	94.1	*33.1*	78.7	0.96	248
					April 2007					
ABS	259.1	**-61.3**	65.7	0.75	240	144.8	13.3	98.1	0.86	240
ATQ	234.3	**-48.4**	57.2	0.65	240	159.0	**49.5**	94.0	0.93	240
BAR	232.0	**-47.1**	55.9	0.62	240	159.5	**47.8**	78.2	0.97	240
CAB	309.4	**-23.5**	32.1	0.74	240	220.3	40.5	96.8	0.96	240
FPE	276.2	**-31.7**	43.8	0.71	240	222.2	*52.2*	123.1	0.94	240
PAY	297.4	**-28.1**	36.8	0.52	240	241.7	36.7	95.2	0.97	240
SOD	NA	NA	NA	NA	NA	156.7	18.5	82.2	0.92	240
SUM	NA	NA	NA	NA	NA	188.1	*3.7*	51.2	0.96	240
SXF	281.6	**-23.5**	36.1	0.86	240	235.7	*57.2*	131.5	0.94	202
TAT	324.9	**-52.1**	59.4	0.54	240	180.3	**110.3**	212.5	0.87	240
XIA	288.5	**-19.7**	28.8	0.79	240	225.8	*71.9*	142.0	0.95	240
					July 2007					
ABS	330.0	**-54.1**	59.1	0.46	247	198.2	14.5	143.5	0.78	248
ATQ	321.7	**-39.1**	48.5	0.10	248	263.2	**74.0**	124.4	0.91	248
BAR	301.1	**-40.2**	49.1	0.08	248	244.7	**96.7**	141.3	0.90	248
CAB	360.1	**-42.1**	48.2	0.60	225	185.0	**95.0**	211.8	0.80	225
FPE	373.1	**-15.9**	25.3	0.81	248	275.1	*65.0*	153.6	0.92	248
PAY	348.2	**-47.0**	55.9	0.40	248	240.0	12.9	176.9	0.84	248
SOD	NA	NA	NA	NA	NA	166.8	**59.7**	155.0	0.78	248
SUM	NA	NA	NA	NA	NA	327.6	*36.8*	88.7	0.94	248
SXF	367.4	−1.0	17.1	0.85	248	294.7	70.4	142.3	0.94	248
TAT	410.4	**-26.1**	30.9	0.57	248	146.3	**110.4**	228.5	0.82	248
XIA	396.6	−4.4	23.1	0.65	248	212.0	**123.8**	210.5	0.92	248
					October 2007					
ABS	263.0	**-36.6**	64.6	0.47	248	27.9	*-9.7*	35.6	0.78	248
ATQ	NA	NA	NA	NA	NA	NA	NA	NA	NA	NA
BAR	274.2	**-74.2**	77.1	0.44	184	15.0	**11.8**	30.5	0.92	243
CAB	330.2	**-47.7**	55.7	0.50	212	78.4	*40.8*	97.8	0.87	212
FPE	284.5	**-27.5**	40.7	0.51	246	104.7	*30.3*	75.3	0.94	246
PAY	321.1	**-50.1**	60.7	0.37	191	101.2	*33.8*	116.3	0.84	248
SOD	NA	NA	NA	NA	NA	24.8	0.4	25.5	0.89	248
SUM	NA	NA	NA	NA	NA	16.7	−3.0	21.8	0.80	248
SXF	312.6	**-26.2**	40.4	0.77	248	124.1	28.8	80.5	0.94	248
TAT	353.9	**-41.1**	48.3	0.66	248	127.2	**55.3**	138.4	0.88	248
XIA	297.7	**-20.7**	32.3	0.82	248	120.4	**52.1**	123.4	0.92	248

[a]Abbreviations for the station names are provided in Table 1. OBS refers to the observed average LW and SW radiation at the surface for each month indicated. r is the correlation between 3 h simulated and observed time series of LW and SW radiation at the surface, and NUM is the number of total 3 h comparisons made based on observed radiation availability for each month. Indices that are italicized boldface indicate biases are statistically significant at 90% confidence level, just italicized for 95%, and just boldfaced for 99%.

the model is given ample opportunity to predict 'clouds'. The CFreq method results in increased CF throughout the entire domain. Over the NSA however, model CFreq is still lower than both MODIS and CloudSat/CALIPSO. After increasing the CF threshold from zero to 0.1 in order to qualify as a cloudy event, CFreq throughout the entire domain substantially decreases (not shown). Therefore, only with the most conservative approach to estimating clouds does the model behave similarly to satellite observations of cloud cover. This deficient cloud cover in the model for July

results in the large anomalous diurnal cycle of 2 m temperature (Part I) and the excessive incident SW and deficit downwelling LW radiation at the surface discussed in the following section.

6. Surface Radiation

[30] Incoming radiation at the surface has been addressed at select locations in previous Polar WRF development studies including the Greenland ice sheet and along the
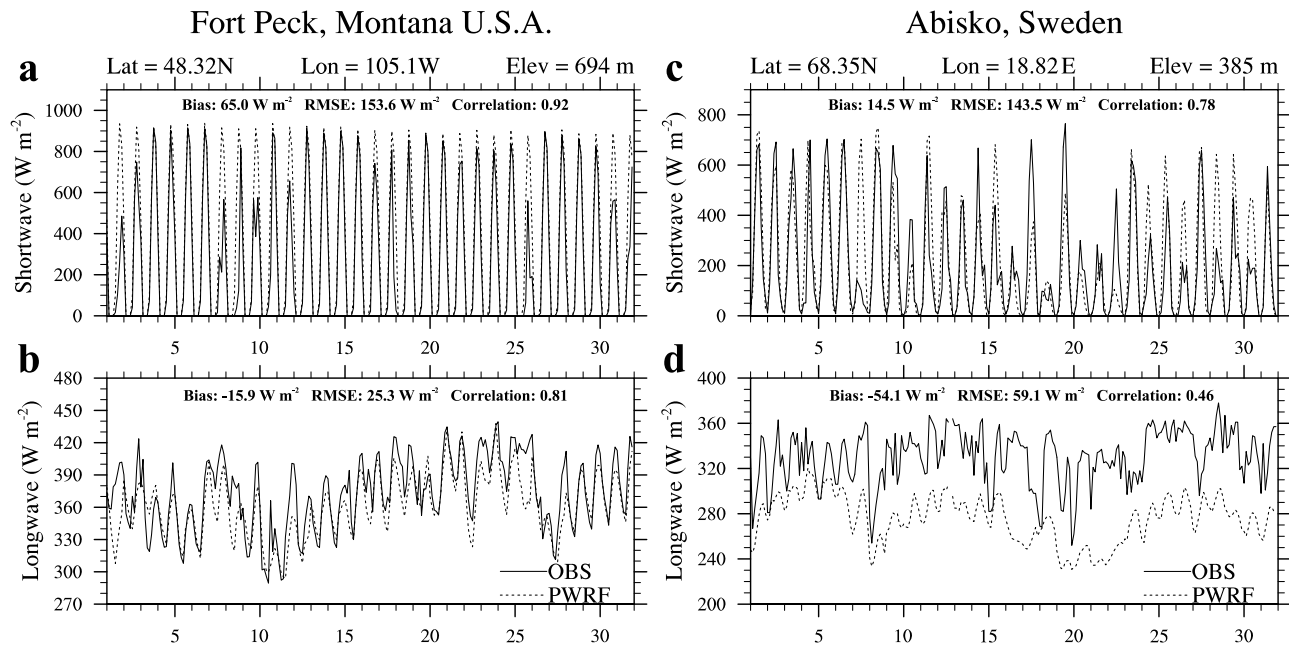
Figure 10. Time series of Polar WRF (black-dashed) and observed (black-solid) (a and c) incoming SW radiation (W m^{-2}) at the surface and (b and d) downwelling LW radiation (W m^{-2}) at the surface for July 2007 for Fort Peck, Montana U.S.A. (Figures 10a and 10b) and Abisko, Sweden (Figures 10c and 10d). Note vertical scales are not the same for each station.

NSA. The investigation of LW and SW radiation is expanded here to include three additional sites in the Arctic (Abisko, Sweden/tundra, Ny-Ålesund, Svalbard/tundra, and Sodankylä, Finland/boreal forest) as well as several stations from the midlatitudes in the domain. LW and SW radiation observations described in Section 3 are compared to the model for the middle months representing each season (January, April, July, and October). Table 4 shows the biases, root-mean square error (RMSE), and correlations for all sites for all four months except for Ny-Ålesund, Svalbard where no comparable model grid point can be found at 60 km. Bias is calculated monthly mean of all 3 h differences in LW and SW radiation.

[31] A student's t-test reveals the biases in LW radiation are statistically significant at 99% for all stations in all months except for Sioux Falls, South Dakota and Xianghe, China in July. Biases range from −62.8 to −1.0 W m^{-2} for stations in the midlatitudes and from −74.2 to −36.6 W m^{-2} for stations in the polar region. Correlations are generally higher in the midlatitudes than in the polar region as well, and for almost all stations July correlations of LW are the lowest of any month. For SW, the biases are typically positive with a distinct seasonality. The lowest biases are generally found in January (low sun angle) and increase to the highest values in July (high sun angle). Likewise, the biases are not as statistically significant as the LW radiations biases, but many stations exhibit statistically significant differences in July. Correlations are generally higher for all months at all locations for SW radiation compared to LW radiation, a reflection of the close link between SW radiation and the diurnal cycle.

[32] Figures 10a and 10b show the 3 h time series plot of SW and LW radiation for Fort Peck, Montana (grassy flat

location in the upper Great Plains). The maximum incident SW radiation is often overpredicted by the model, yielding a monthly mean bias of 65.0 W m^{-2}. However, the correlation between model and observations is high at 0.92. The LW radiation is underpredicted (−15.9 W m^{-2}), with a good correlation of 0.81. Surface air temperature analysis (Part I) shows an average 3°C mean temperature bias for July for stations in this region, which is consistent with the positive SW bias, deficit in the LW radiation, and too little cloud. Particularly on July 1, 7, 11, and 25, the SW bias is strongly positive and corresponds to large negative LW radiation biases giving further indication that the effects of clouds on the radiation are not well represented during these events.

[33] For the polar region, SW and LW radiation for July is shown for Abisko, Sweden (flat tundra surface) located approximately 200 km north of the Arctic Circle (Figures 10c and 10d). While SW radiation is overpredicted, the bias is less than at other Arctic sites (+14.5 W m^{-2}). Abisko is situated just south of a large lake and the terrain rises quickly to the south and west to over 1700 m (www.linnea.com/∼ans/). Southerly and westerly winds in this region will produce down-sloping winds that work to dissipate clouds. This typically results in clearer conditions than would be expected at sites along the NSA and as such, the SW biases are smaller in this simulation. There is a large deficit in the LW radiation as shown in Table 4. Even on July 17 and 19 when the SW radiation is substantially underpredicted by the model (a result of a poorly modeled down-sloping event), the large negative biases in the LW during these events suggests very little cloud effects on radiation are realized and the correlation is greatly reduced. Again, these plots support the conclusion cloud radiative effects over land in the summer are not well represented.
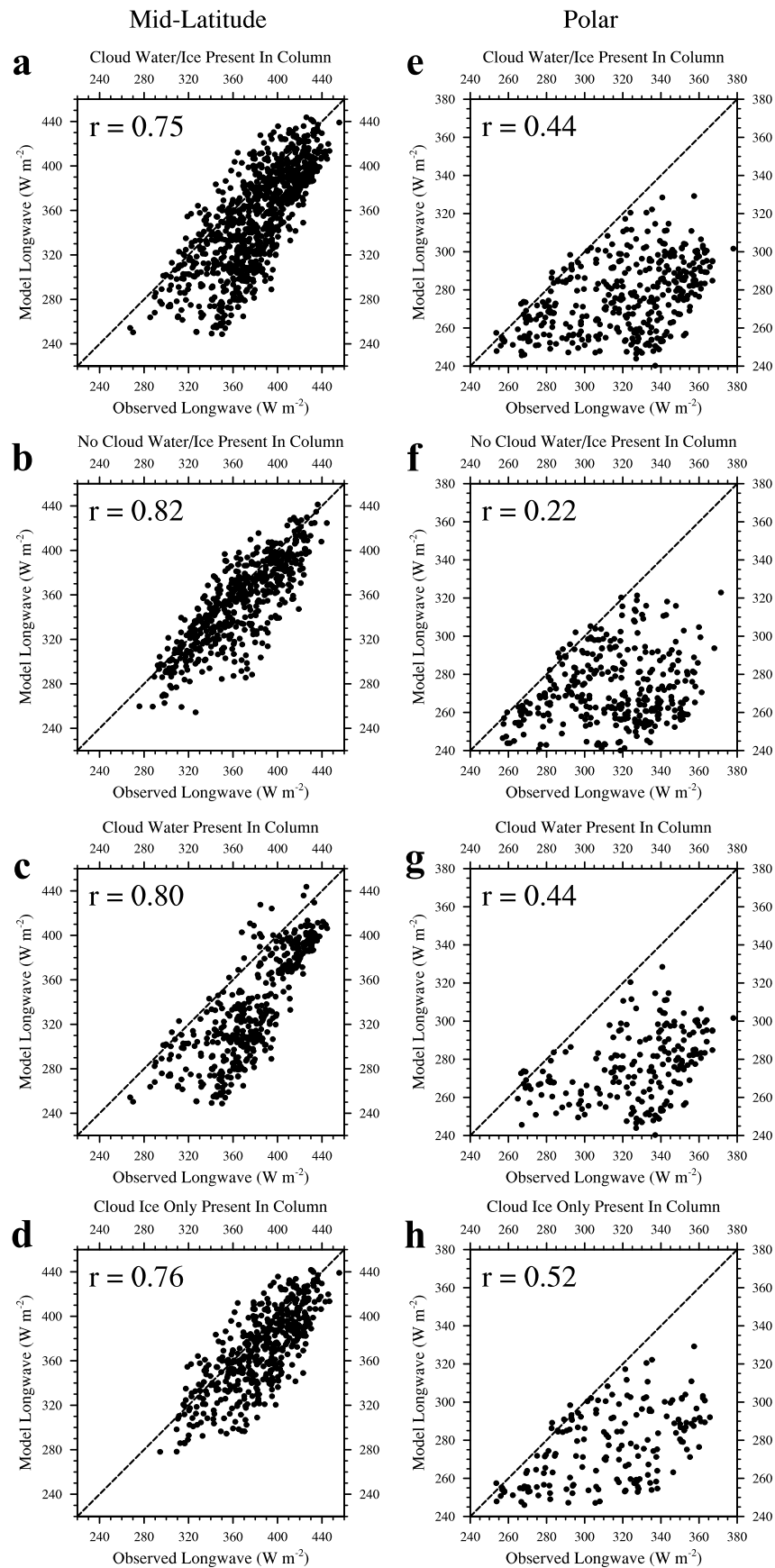
Figure 11

This result appears to be insensitive to surface type as similar results of SW radiation biases are found for the boreal site Sodankylä, Finland.

[34] Figure 11 shows scatterplots of 3 h model LW radiation versus observed LW radiation for July 2007 for the midlatitude (six stations) and polar region (three stations) under varying conditions of model cloud species availability (cloud water and/or cloud ice available (Figure 11a), no cloud water or cloud ice (Figure 11b), cloud water available regardless of cloud-ice availability (Figure 11c), and cloud ice only (Figure 11d)). For the midlatitudes, correlations are fairly strong for all four cases considered with subtle differences to note. First, when cloud water and/or cloud ice is present in the vertical column, the model biases are negative supporting the findings in Table 4 (Figure 11a). Under presumed "clear sky" conditions when no cloud water or cloud ice is present, the correlation increases and the model and observations are in better agreement (Figure 11b). When cloud water is present regardless of cloud-ice conditions, the performance of LW is impacted and the bias is strongly negative (Figure 11c). A greater negative LW bias even when the model shows cloud water implies the cloud water effects on LW radiation are not well represented in the model, as LW radiation should increase when cloud water is present. An examination of the RRTM LW radiation scheme shows that cloud effects on radiation are operated in a switch mode. When the sum of the cloud water and cloud ice at each vertical level exceeds a set threshold, then cloud fraction is set to unity at that level. Otherwise, the cloud fraction is set to zero. If only cloud ice is present, there is zero effect on the cloud fraction at that level. Consistent with this setting, Figure 11d shows reasonable agreement between model LW and observed LW under ice only conditions in the model. The decrease in the correlation between "cloud-free" and ice only is likely a result of cloud ice having a small net effect on radiation in the observations while having no effect in the model. For the polar region, it is clear the performance of model LW radiation suffers greatly compared to observations as the correlations are much lower in all four cases considered. In all situations, the biases in the LW radiation are negative, with an apparent insensitivity between cloud water/cloud ice conditions and "clear sky." This insensitivity to cloud water and/or cloud ice in the polar region is exemplified by Figures 10c and 10d where the LW radiation bias at Abisko, Sweden is negative throughout the month of July.

[35] This finding is further supported by the difference between model and observed correlations of SW versus LW radiation. Not surprisingly many observed stations show a negative correlation, an indication that as clouds increase, the amount of SW reaching the surface decreases (vice versa for LW radiation). However, the correlations between SW and LW for all stations in the model are positive. At Fort Peck and Sioux Falls, South Dakota, positive correlations between SW and LW radiation are supported by the

observations. For these stations, the model shows little cloud water in the column throughout July leading to a positive correlation between SW and LW radiation and an overall accurate prediction. However, for stations such as Atqasuk, Alaska where cloud water is also not present in the model atmosphere, the resulting positive correlation of 0.55 is opposite to the observed correlation of −0.22 and a poor prediction of LW results. This evidence suggests that more cloud water is needed in the model simulation, especially in the Arctic, so that cloud effects on radiation are more representative of observations.

[36] While Figure 11 demonstrates that the model often fails to produce clouds, Figure 12 shows model versus observed SW and LW radiation at Barrow, Alaska for July 2007 when the model and observations agree on cloud conditions. A cloudy model state is defined as a CF greater than zero using equation (1), and an observed cloudy state is any cloud observation not reported as clear. Only 84 out of 248 observations for the month of July 2007 agree with the model. For both the cloudy and clear state, the model overpredicts the SW radiation and underpredicts the LW radiation. Even when the model correctly predicts clouds, the radiation produced in the model is biased (positive SW/ negative LW) indicating the radiation schemes are not adequately producing cloud radiative effects in the model. This evidence suggests that the model clouds are too optically thin with too little cloud liquid water, which agrees well with Figure 11 and previous WRF modeling studies of clouds in the Arctic [e.g., *Solomon et al.*, 2009]. Following a similar investigation by *Hines et al.* [2011], Barrow is compared to a model grid point much further inland. Here, the SW radiation results remain the same with too much SW radiation predicted for the month. However, the LW radiation bias is smaller and less negative indicating that although the original comparison for Barrow (represented more like an ocean point) is valid, the model LW radiation behavior is likely to fall between what is shown in Figures 12c and 12d and this inland land point (not shown).

[37] To test whether or not the above evidence is simply a result of the physics parameterizations chosen, additional sensitivity simulations are conducted for July 2007. First, the updated RRTMG LW radiation scheme is used [*Iacono et al.*, 2008]. Here the RRTM scheme has been updated to improve computer efficiency and sub-grid scale cloud variability particularly in Global Climate Models (GCMs). Not only does this scheme rely on cloud water and cloud-ice mixing ratio threshold at each level, but it also considers saturation based on relative humidity at each level. Another test maintains the original RRTM LW scheme while switching from the WRF 6-class to the Morrison microphysics scheme, as this double-moment scheme is thought to physically represent clouds in a more explicit manner. In both cases, predictions of model LW are not improved in any of the cloud species cases described above. A third sensitivity examines the QVAPOR simulation used to improve the

Figure 11. Scatterplots of model versus observed LW radiation for July 2007 under the following model conditions: (a and e) cloud water and/or cloud ice present in the vertical column, (b and f) no cloud water or cloud ice in the vertical column, (c and g) cloud water in the vertical column regardless of cloud ice, and (d and h) cloud ice only in the vertical column for midlatitude region (Figures 11a, 11b, 11c, and 11d; six stations combined) and polar region (Figures 11e, 11f, 11g, and 11h; three stations combined).

Barrow, Alaska
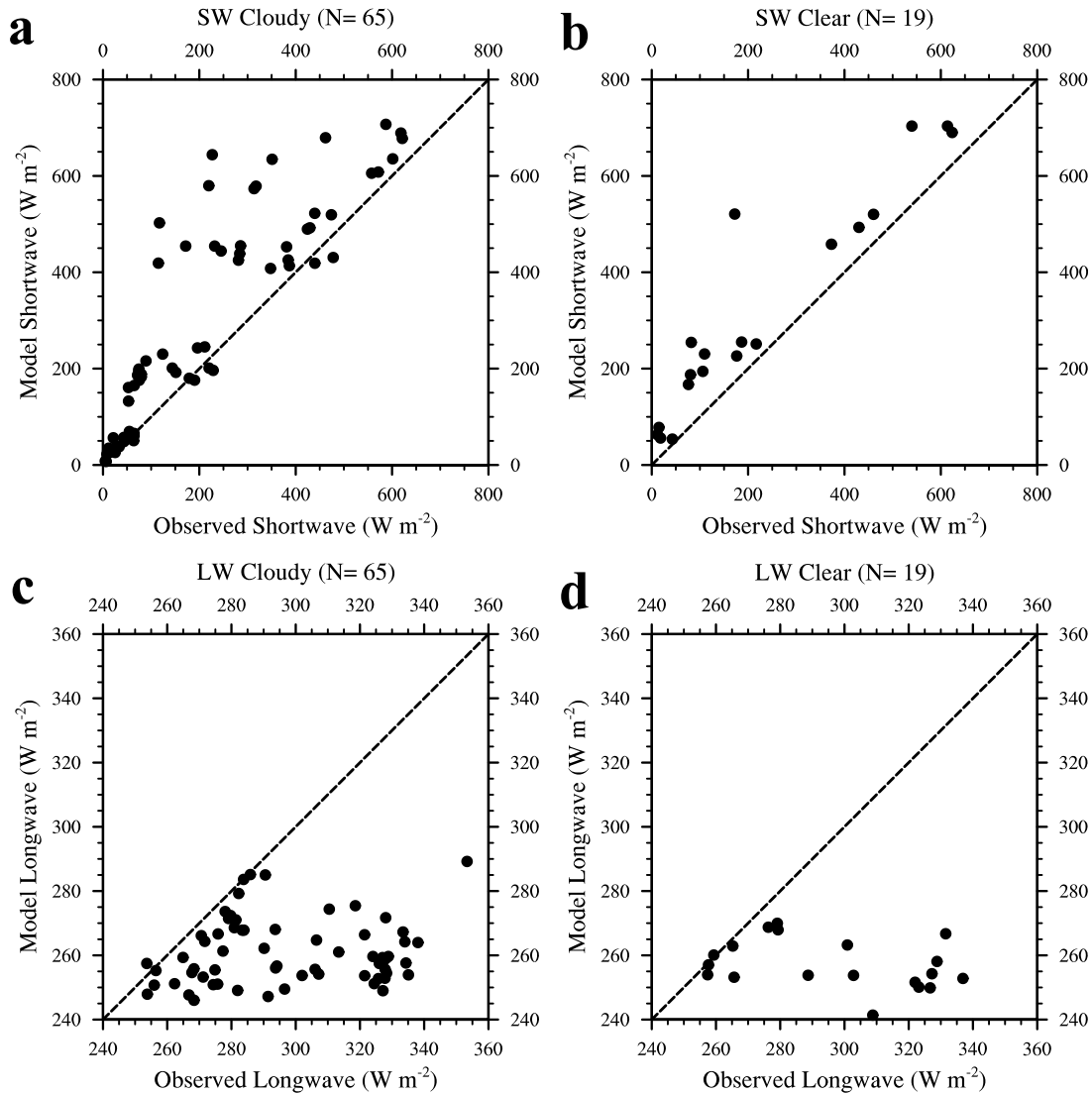
Figure 12. Model versus observed (a) SW radiation when both model and observations are cloudy, (b) SW radiation when both model and observations are clear, (c) LW radiation when both model and observations are cloudy, and (d) LW radiation when both model and observations are clear for Barrow, Alaska during July 2007. N represents the number of cases out of 248 for the month that the model and observations agree for each case.

convective precipitation as described in Section 4.2. Interestingly, analysis of CF shows higher CF over open water areas of the Arctic Ocean (e.g., Beaufort Sea, Laptev Sea, Kara Sea, etc) and the adjacent land areas such as the NSA. However, this simulation fails to improve the biases in SW and LW radiation for the sites selected in this study.

[38] Through personal communication with Wayne Angevine of the NOAA Earth System Research Laboratory along with the conclusions drawn from *Hines et al.* [2011], the lack of clouds throughout the domain appears to be an issue with subgrid-scale non-precipitating clouds. While this investigation reveals that changing the microphysics scheme has little impact in CF across the entire Arctic, *Hines et al.* [2011] found that clouds and radiation over the Arctic

Ocean are sensitive to the selection of microphysics schemes at a selected ocean site near Barrow, Alaska. However, those results were not extended to the entire western Arctic domain and cannot be immediately compared to the current study. *Hines et al.* [2011] do suggest from analyzing the relative humidity profiles that excessive mixing of water vapor in the vertical inhibits moisture availability for low clouds. This evidence, along with the poor performance of LW radiation at the surface in this study strongly suggests the immediate need for improvements to physics parameterizations in the polar regions as it relates to model cloud development across the Arctic. This includes improving the temporal development of clouds in the model, a better representation of the cloud radiative effects due to cloud water

in the atmospheric column, and improving the moisture fluxes into the boundary layer.

7. Conclusions

[39] This paper has investigated the performance of Polar WRF forecasts of precipitation, clouds, and downwelling radiation on the broad scale over the ASR domain. Annual mean precipitation comparison to ERA-Interim reveals Polar WRF is spatially consistent with this data set. The wettest areas coincide with the Atlantic and Pacific storm-track regions. Likewise, the driest areas can be found in the Arctic and the deserts of Eurasia. Overall mean biases of annual precipitation compared to station precipitation measurements are small, but Polar WRF shows a positive bias especially in the midlatitudes during spring and summer when convective precipitation is dominant. Decreasing boundary layer water vapor in a nudged simulation results in less convective precipitation and reduced total precipitation biases. This discovery indicates the model is becoming too moist in the lower troposphere, and the inclusion of the data assimilation in ASR will improve precipitation. Using a diagnostic equation for calculating model CF, it appears that CF is underpredicted by the model especially in July 2007. When CF is used to compute a CFreq, where the threshold for clouds is set conservatively low, the model approaches observations depicted by MODIS and CloudSat/CALIPSO. However, areas of particular interest such as the NSA still appear to suffer from a lack of clouds. Finally, model performance of radiation reveals an excess of SW and a deficit of LW radiation at many sites throughout the domain, supporting the findings from the CF analysis. A key finding for the development of Polar WRF is its inability to predict accurately LW radiation as a function of the amount of cloud water or cloud ice in the model atmosphere, especially for the Arctic.

[40] As a synthesis with Part I, the results demonstrated here show that the anomalous diurnal 2 m temperature range is a likely result of deficient cloud-radiative effects in the model. Warmer daytime temperatures due to excessive SW radiation and increases in the energy available at the surface to evaporate moisture into the boundary layer lead to high evaporation rates found for July. The increased evaporation near the surface and higher relative humidity leads to increased precipitation, especially during warm season convection. However, this increase in near-surface moisture does not translate into an increase in cloud cover effects on radiation, seen particularly in the downwelling LW radiation biases at the surface.

[41] Overall, the performance of the short-term forecasts from Polar WRF bode well for its use as ASR's primary model. Moving forward however, attention must be given to resolve outstanding issues with cloud microphysics and radiation. The consensus from a recent workshop on the use of WRF in polar regions at the Ohio State University in November 2011 (http://polarmet.osu.edu/workshops/pwrf_2011/) highlights the need for improving Polar WRF forecasts of clouds and their radiative effects, not only for high resolution modeling of single events, but also across pan-Arctic domains and simulations on longer time scales. This includes resolving radiation and aerosol concentration parameterizations among the various physics schemes, which also emphasizes the need for additional observations from field campaigns.

References

Ackerman, S. A., R. E. Holz, R. Frey, E. W. Eloranta, B. C. Maddux, and M. McGill (2008), Cloud detection with MODIS. Part II: Validation, *J. Atmos. Oceanic Technol.*, 25, 1073–1086, doi:10.1175/2007JTECHA1053.1.

Ackerman, T., and G. Stokes (2003), The Atmospheric Radiation Measurement Program, *Phys. Today*, 56, 38–45, doi:10.1063/1.1554135.

Adler, R. F., et al. (2003), The Version-2 Global Precipitation Climatology Project (GPCP) monthly precipitation analysis (1979-present), *J. Hydrometeorol.*, 4, 1147–1167, doi:10.1175/1525-7541(2003)004<1147:TVGPCP>2.0.CO;2.

Arctic Research Consortium of the United States (2005), Study of environmental Arctic change: Plans for implementation during the International Polar Year and beyond, report, 104 pp., ARCUS, Fairbanks, Alaska.

Augustine, J. A., J. J. DeLuisi, and C. N. Long (2000), SURFRAD—A national surface radiation budget network for atmospheric research, *Bull. Am. Meteorol. Soc.*, 81, 2341–2357, doi:10.1175/1520-0477(2000)081<2341:SANSRB>2.3.CO;2.

Augustine, J. A., G. B. Hodges, C. R. Cornwall, J. J. Michalsky, and C. I. Medina (2005), An update on SURFRAD—The GCOS surface radiation budget network for continental United States, *J. Atmos. Oceanic Technol.*, 22, 1460–1472, doi:10.1175/JTECH1806.1.

Barstad, I., A. Sorteberg, F. Flatøy, and M. Déqué (2009), Precipitation, temperature and wind in Norway: Dynamical downscaling of ERA-40, *Clim. Dyn.*, 33, 769–776, doi:10.1007/s00382-008-0476-5.

Brimelow, J. C., and G. W. Reuter (2008), Moisture sources for extreme rainfall events over the Mackenzie River Basin, in *Cold Region and Hydrologic Studies: The Mackenzie GEWEX Experience*, vol. 1, *Atmospheric Dynamics*, edited by M.-K. Woo, pp. 127–136, Springer, Berlin.

Bromwich, D. H., K. M. Hines, and L.-S. Bai (2009), Development and testing of Polar WRF: 2. Arctic Ocean, *J. Geophys. Res.*, 114, D08122, doi:10.1029/2008JD010300.

Bromwich, D. H., Y.-H. Kuo, M. Serreze, J. Walsh, L.-S. Bai, M. Barlage, K. M. Hines, and A. Slater (2010), Arctic System Reanalysis: Call for community involvement, *Eos Trans. AGU*, 91(2), 13–14, doi:10.1029/2010EO020001.

Cassano, J. J., J. E. Box, D. H. Bromwich, L. Li, and K. Steffen (2001), Evaluations of Polar MM5 simulations of Greenland's atmospheric circulation, *J. Geophys. Res.*, 106(D24), 33,867–33,889, doi:10.1029/2001JD900044.

Cassano, J. J., M. E. Higgins, and M. W. Seefeldt (2011), Performance of the Weather Research and Forecasting (WRF) Model for month-long pan-Arctic simulations, *Mon. Weather Rev.*, 139, 3469–3488, doi:10.1175/MWR-D-10-05065.1.

Chen, F., and J. Dudhia (2001), Coupling an advanced land surface-hydrology model with the Penn State-NCAR MM5 modeling system. Part I. Model and implementation and sensitivity, *Mon. Weather Rev.*, 129, 569–585, doi:10.1175/1520-0493(2001)129<0569:CAALSH>2.0.CO;2.

Chou, M.-D., and M. J. Suarez (1994), An efficient thermal infrared radiation parameterization for use in general circulation models, *NASA Tech. Memo.*, TM-104606, 85 pp.

Colle, B. A., K. J. Westrick, and C. F. Mass (1999), Evaluation of MM5 and Eta-10 precipitation forecasts over the Pacific Northwest during the cool season, *Weather Forecast.*, 14, 137–154, doi:10.1175/1520-0434(1999)014<0137:EOMAEP>2.0.CO;2.

Comiso, J. (1999), Bootstrap sea ice concentrations from Nimbus-7 SMMR and DMSP SSM/I, January 1, 2007 to January 1, http://nsidc.org/data/nsidc-0079.html, Natl. Snow and Ice Data Cent., Boulder, Colo. (updated 2008).

Curry, J. A., W. B. Rossow, D. Randall, and J. L. Schramm (1996), Overview of Arctic cloud and radiation characteristics, *J. Clim.*, 9, 1731–1764, doi:10.1175/1520-0442(1996)009<1731:OOACAR>2.0.CO;2.

Devine, K. A., and È. Mekis (2008), Field accuracy of Canadian rain measurements, *Atmos. Ocean*, 46(2), 213–227, doi:10.3137/ao.460202.

Easterling, D. R., and T. C. Peterson (1995), A new method for detecting undocumented discontinuities in climatological time series, *Int. J. Climatol.*, 15, 369–377, doi:10.1002/joc.3370150403.

Fogt, R. L., and D. H. Bromwich (2008), Atmospheric moisture and cloud cover characteristics forecast by AMPS, *Weather Forecast.*, 23, 914–930, doi:10.1175/2008WAF2006100.1.

Frey, R. A., S. A. Ackerman, Y. Liu, K. I. Strabala, H. Zhang, J. R. Key, and X. Wang (2008), Cloud detection with MODIS. Part I: Improvements in the MODIS cloud mask for collection 5, *J. Atmos. Oceanic Technol.*, 25, 1057–1072, doi:10.1175/2008JTECHA1052.1.

Gemmill, W., B. Katz, and X. Li (2007), Daily real-time global sea surface temperature-high resolution analysis at NOAA/NCEP, *NCEP Off. Note 260*, 39 pp., NCEP, Camp Springs, Md.

Grell, G. A., and D. Devenyi (2002), A generalized approach to parameterizing convection combining ensemble and data assimilation techniques, *Geophys. Res. Lett.*, 29(14), 1693, doi:10.1029/2002GL015311.

Hack, J. J., B. A. Boville, B. P. Briegleb, J. T. Kiehl, P. J. Rasch, and D. L. Williamson (1993), Description of the NCAR Community Climate Model (CCM2), *NCAR/TN-382+STR*, 108 pp., Natl. Cent. for Atmos. Res., Boulder, Colo.

Hegner, H., G. Müller, V. Nespor, A. Ohmura, R. Steigrad, and H. Gilgen (1998), World Climate Research Program WCRP (WMO/ICSU/IOC) Baseline Surface Radiation Network (BSRN): Update of the technical plan for BSRN data management, *Tech. Rep. 2 Vers. 1.0.*, 34 pp., World Radiat. Monit. Cent., Alfred Wegener Inst., Bremerhaven, Germany.

Hines, K. M., and D. H. Bromwich (2008), Development and testing of Polar WRF. Part I: Greenland ice sheet meteorology, *Mon. Weather Rev.*, 136, 1971–1989, doi:10.1175/2007MWR2112.1.

Hines, K. M., D. H. Bromwich, L.-S. Bai, M. Barlage, and A. G. Slater (2011), Development and testing of Polar WRF. Part III: Arctic land, *J. Clim.*, 24, 26–48, doi:10.1175/2010JCLI3460.1.

Hong, S.-Y., and J.-O. Lin (2006), The WRF single-moment 6-class microphysics scheme (WSM6), *J. Korean Meteorol. Soc.*, 42(2), 129–151.

Hubanks, P. A., M. D. King, S. A. Platnick, and R. A. Pincus (2008), MODIS atmosphere L3 gridded product algorithm theoretical basis document, *ATBD-MOD-30*, 96 pp., NASA Goddard Space Flight Cent., Greenbelt, Md. [Available at http://modis-atmos.gsfc.nasa.gov/MOD08_D3/atbd.html.]

Iacono, M. J., J. S. Delamere, E. J. Mlawer, M. W. Shephard, S. A. Clough, and W. D. Collins (2008), Radiative forcing by long-lived greenhouse gases: Calculations with AER radiative transfer models, *J. Geophys. Res.*, 113, D13103, doi:10.1029/2008JD009944.

Janjić, Z. I. (2002), Nonsingular implementation of the Mellor-Yamada level 2.5 scheme in the NCEP Meso model, *NCEP Off. Note 437*, 61 pp., NCEP, Camp Springs, Md.

Kain, J. S. (2004), The Kain-Fritsch convective parameterization: An update, *J. Appl. Meteorol.*, 43, 170–181, doi:10.1175/1520-0450(2004)043<0170:TKCPAU>2.0.CO;2.

Kain, J. S., and J. M. Fritsch (1990), A one-dimensional entraining/detraining plume model and its application in convective parameterization, *J. Atmos. Sci.*, 47, 2784–2802, doi:10.1175/1520-0469(1990)047<2784:AODEPM>2.0.CO;2.

Kain, J. S., and J. M. Fritsch (1993), Convective parameterization for mesoscale models: The Kain-Fritsch scheme, in *The Representation of Cumulus Convection in Numerical Models*, edited by K. A. Emanuel and D. J. Raymond, pp. 165–170, Am. Meteorol. Soc., Boston, Mass.

Kay, J. E., and A. Gettelman (2009), Cloud influence on and response to seasonal Arctic sea ice loss, *J. Geophys. Res.*, 114, D18204, doi:10.1029/2009JD011773.

Kay, J. E., T. L'Ecuyer, A. Gettelman, G. Stephens, and C. O'Dell (2008), The contribution of cloud and radiation anomalies to the 2007 Arctic sea ice extent minimum, *Geophys. Res. Lett.*, 35, L08503, doi:10.1029/2008GL033451.

Kipeläinen, T., T. Vihma, and H. Ólafsson (2011), Modelling of spatial variability and topographic effects over Arctic fjords in Svalbard, *Tellus, Ser. A*, 63, 223–237, doi:10.1111/j.1600-0870.2010.00481.x.

Lo, J. C.-F., Z.-L. Yang, and R. A. Pielke Sr. (2008), Assessment of three dynamical climate downscaling methods using the Weather Research and Forecasting (WRF) model, *J. Geophys. Res.*, 113, D09112, doi:10.1029/2007JD009216.

Mace, G. G., Q. Zhang, M. Vaughan, R. Marchand, G. Stephens, C. Trepte, and D. Winkler (2009), A description of hydrometeor layer occurrence statistics derived from the first year of merged CloudSat and CALIPSO data, *J. Geophys. Res.*, 114, D00A26, doi:10.1029/2007JD009755.

Mäkiranta, E., T. Vihma, A. Sjöblom, and E.-M. Tastula (2011), Observations and modeling of the atmospheric boundary layer over sea-ice in a Svalbard fjord, *Boundary Layer Meteorol.*, 140, 105–123, doi:10.1007/s10546-011-9609-1.

Mekis, È. (2005), Adjustments for trace measurements in Canada, paper presented at 15th Conference on Applied Climatology, Am. Meteorol. Soc., Savannah, Ga.

Mekis, È., and W. D. Hogg (1999), Rehabilitation and analysis of Canadian daily precipitation time series, *Atmos. Ocean*, 37(1), 53–85, doi:10.1080/07055900.1999.9649621.

Mekis, È., and R. Hopkinson (2004), Derivation of an improved snow water equivalent adjustment factor map for application on snowfall ruler measurements in Canada, paper presented at 14th Conference on Applied Climatology, Am. Meteorol. Soc., Seattle, Wash.

Mlawer, E. J., S. J. Taubman, P. D. Brown, M. J. Iacono, and S. A. Clough (1997), Radiative transfer for inhomogeneous atmosphere: RRTM, a validated correlated-k model for the longwave, *J. Geophys. Res.*, 102(D14), 16,663–16,682, doi:10.1029/97JD00237.

Mölders, N., and G. Kramm (2010), A case study on wintertime inversions in interior Alaska with WRF, *Atmos. Res.*, 95, 314–332, doi:10.1016/j.atmosres.2009.06.002.

Mölders, N., M. Laube, and E. Raschke (1995), Evaluation of model generated cloud cover by means of satellite data, *Atmos. Res.*, 39, 91–111, doi:10.1016/0169-8095(94)00059-M.

Morrison, H., and J. O. Pinto (2006), Intercomparison of bulk microphysics schemes in mesoscale simulations of springtime Arctic mixed-phase stratiform clouds, *Mon. Weather Rev.*, 134, 1880–1900, doi:10.1175/MWR3154.1.

Morrison, H., J. A. Curry, and V. I. Khvorostayanov (2005), A new double-moment microphysics parameterization for application in cloud and climate models. Part I: Description, *J. Atmos. Sci.*, 62, 1665–1677, doi:10.1175/JAS3446.1.

Morrison, H., G. Thompson, and V. Tatarskii (2009), Impact of cloud microphysics on the development of trailing stratiform precipitation in a simulated squall line: Comparison of one- and two-moment schemes, *Mon. Weather Rev.*, 137, 991–1007, doi:10.1175/2008MWR2556.1.

Neiman, P. J., F. M. Ralph, A. B. White, D. E. Kingsmill, and P. O. G. Perrson (2002), The Statistical relationship between upslope flow and rainfall in California's coastal mountains: Observations during CALJET, *Mon. Weather Rev.*, 130, 1468–1492, doi:10.1175/1520-0493(2002)130<1468:TSRBUF>2.0.CO;2.

Nicolas, J. P., and D. H. Bromwich (2011), Climate of West Antarctica and influence of marine air intrusions, *J. Clim.*, 24, 49–67, doi:10.1175/2010JCLI3522.1.

Ohmura, A., et al. (1998), Baseline Surface Radiation Network (BSRN/WCRP): New precision radiometry for climate research, *Bull. Am. Meteorol. Soc.*, 79(10), 2115–2136, doi:10.1175/1520-0477(1998)079<2115:BSRNBW>2.0.CO;2.

Peterson, T. C., and D. R. Easterling (1994), Creation of homogeneous composite climatological reference series, *Int. J. Climatol.*, 14, 671–679, doi:10.1002/joc.3370140606.

Peterson, T. C., and R. S. Vose (1997), An overview of the Global Historical Climatology Network temperature database, *Bull. Am. Meteorol. Soc.*, 78(12), 2837–2849, doi:10.1175/1520-0477(1997)078<2837:AOOTGH>2.0.CO;2.

Serreze, M. C., R. G. Barry, and J. E. Walsh (1995), Atmospheric water vapor characteristics at 70°N, *J. Clim.*, 8, 719–731, doi:10.1175/1520-0442(1995)008<0719:AWVCA>2.0.CO;2.

Serreze, M. C., A. P. Barret, and F. Lo (2005), Northern high-latitude precipitation as depicted by atmospheric reanalyses and satellite retrievals, *Mon. Weather Rev.*, 133, 3407–3430, doi:10.1175/MWR3047.1.

Simmons, A., S. Uppala, D. Dee, and S. Kobayashi (2007), ERA-Interim: New ECMWF reanalysis products from 1989 onwards, *ECMWF Newsl.*, 110, 25–35.

Skamarock, W. C., J. B. Klemp, J. Dudhia, D. Gill, D. Barker, M. Dudhia, X.-Y. Huang, W. Wang, and J. G. Powers (2008), A description of the Advanced Research WRF Version 3, *NCAR/TN-475+STR*, 113 pp., NCAR, Boulder, Colo.

Solomon, A., H. Morrison, P. O. G. Persson, M. Shupe, and J.-W. Bao (2009), Investigation of microphysical parameterizations of snow and ice in Arctic clouds during M-PACE through model-observation comparisons, *Mon. Weather Rev.*, 137, 3110–3128, doi:10.1175/2009MWR2688.1.

Stauffer, D. R., and N. L. Seaman (1990), Use of four-dimensional data assimilation in a limited- area mesoscale model. Part I: Experiments with synoptic-scale data, *Mon. Weather Rev.*, 118, 1250–1277, doi:10.1175/1520-0493(1990)118<1250:UOFDDA>2.0.CO;2.

Steffen, K., J. E. Box, and W. Abdalati (1996), Greenland climate network: GC-Net, in *Special Report on Glaciers, Ice Sheets and Volcanoes*, edited by S. C. Colbeck, *CRREL 96–27*, pp. 98–103, Cold Reg. Res. and Eng. Lab., Hanover, N. H.

Trenberth, K. E., J. T. Fasullo, and J. Mackaro (2011), Atmospheric moisture transports from ocean to land and global energy flows in reanalyses, *J. Clim.*, *24*, 4907–4924, doi:10.1175/2011JCLI4171.1.

Walsh, J. E., W. L. Chapman, and D. H. Portis (2009), Arctic cloud fraction and radiative fluxes in atmospheric reanalyses, *J. Clim.*, *22*, 2316–2334, doi:10.1175/2008JCLI2213.1.

Wendler, G., and F. Eaton (1990), Surface radiation budget at Barrow, Alaska, *Theor. Appl. Climatol.*, *41*, 107–115, doi:10.1007/BF00866433.

White, A. B., P. J. Neiman, F. M. Ralph, D. E. Kingsmill, and P. O. G. Perrson (2003), Coastal orographic rainfall processes observed by radar during the California Land-Falling Jets Experiment, *J. Hydrometeorol.*, *4*, 264–282, doi:10.1175/1525-7541(2003)4<264:CORPOB>2.0.CO;2.

Wilson, A. B., D. H. Bromwich, and K. M. Hines (2011), Evaluation of Polar WRF forecasts on the Arctic System Reanalysis Domain: Surface and upper air analysis, *J. Geophys. Res.*, *116*, D11112, doi:10.1029/2010JD015013.

Yarker, M. B., D. PaiMazumder, C. F. Cahill, J. Dehn, A. Prakash, and N. Mölders (2010), Theoretical investigations on potential impacts of high-latitude volcanic emissions of heat, aerosols, and water vapor and their interactions with clouds and precipitation, *Open Atmos. Sci. J.*, *4*, 24–44, doi:10.2174/1874282301004010024.

D. H. Bromwich, K. M. Hines, and A. B. Wilson, Polar Meteorology Group, Byrd Polar Research Center, Ohio State University, 108 Scott Hall, 1090 Carmack Rd., Columbus, OH 43210, USA. (wilson.1010@buckeyemail.osu.edu)